

1 **New insight into the formation and aging processes of organic**
2 **aerosol from positive matrix factorization (PMF) analysis of**
3 **ambient FIGAERO-CIMS thermograms**

4 Mingfu Cai^{1,2,3}, Bin Yuan^{2,3}, Weiwei Hu^{4,5*}, Ye Chenshuo⁶, Shan Huang^{2,3}, Suxia
5 Yang⁷, Wei Chen⁴, Yuwen Peng^{2,3}, Zhaoxiong Deng^{2,3}, Jun Zhao^{8†}, Duohong Chen⁹,
6 Jiaren Sun¹, Min Shao^{2,3}

7 ¹Guangdong Province Engineering Laboratory for Air Pollution Control, Guangdong Provincial Key
8 Laboratory of Water and Air Pollution Control, South China Institute of Environmental Sciences, MEE,
9 Guangzhou 510655, China

10 ²Institute for Environmental and Climate Research, Jinan University, Guangzhou 511443, China

11 ³Guangdong-Hongkong-Macau Joint Laboratory of Collaborative Innovation for Environmental
12 Quality, Jinan University, Guangzhou 510632, China

13 ⁴ State Key Laboratory of Advanced Environmental Technology, Guangzhou Institute of Geochemistry,
14 Chinese Academy of Sciences, Guangzhou, 510640, China

15 ⁵ Guangdong-Hong Kong-Macao Joint Laboratory for Environmental Pollution and Control,
16 Guangzhou Institute of Geochemistry, Chinese Academy of Science, Guangzhou, China

17 ⁶ Guangdong Provincial Academy of Environmental Science, Guangzhou, 510045, China

18 ⁷ Guangzhou Research Institute of Environment Protection Co.,Ltd, Guangzhou 510620, China

19 ⁸School of Atmospheric Sciences, Guangdong Province Key Laboratory for Climate Change and
20 Natural Disaster Studies, and Institute of Earth Climate and Environment System, Sun Yat-sen
21 University, Zhuhai 519082, China

22 ⁹Guangdong Environmental Monitoring Center, Guangzhou 510308, China

23 [†]Deceased, 10/2024

24

25 Correspondence to: Weiwei Hu (weiwei@gig.ac.cn)

26

27 **Abstract**

28 Secondary organic aerosol (SOA) is an important component of organic aerosol (OA), yet its
29 atmospheric evolution and impacts on volatility remain poorly understood. In this study, we
30 investigated the volatility of different types of SOA at a downwind site of the Pearl River Delta
31 (PRD) region in the fall of 2019, using a time-of-flight chemical ionization mass spectrometer
32 coupled with a Filter Inlet for Gases and Aerosol (FIGAERO-CIMS). Positive matrix factorization
33 (PMF) analysis was performed on the thermogram data of organic compounds (referred as
34 FIGAERO-OA) measured by the FIGAERO-CIMS. Eight factors were resolved, including six
35 daytime chemistry related factors, a biomass burning related factor (BB-LVOA, 10% of the
36 FIGAERO-OA), and a nighttime chemistry related factor (Night-LVOA, 15%) along with their
37 corresponding volatility. Day-HNO_x-LVOA (12%) and Day-LNO_x-LVOA (11%) were mainly
38 formed through gas-particle partitioning. Increasing NO_x levels mainly affected SOA formation
39 through gas-particle partitioning, suppressing the formation of low-volatile organic vapors, and thus
40 promoting the formation of relatively high volatile OA with a higher N:C ratio. Two aged OA factors,
41 Day-aged-LVOA (16%) and Day-aged-ELVOA (11%), were attributed to daytime photochemical
42 aging of pre-existing OA. In addition, the daytime formation of Day-urban-LVOA (16%) and Day-
43 urban-ELVOA (7%) could only be observed in the urban plume. Results show that both gas-particle
44 partitioning (36%) and photochemical aging (30%) accounted for a major fraction in FIGAERO-
45 OA in the afternoon during the urban air masses period, especially for high-NO_x-like pathway
46 (~21%). In general, the six daytime OA factors collectively explain the majority (82%) of daytime
47 SOA identified by an aerosol mass spectrometer (AMS). While BB-LVOA and Night-LVOA
48 accounted for 13% of biomass burning OA and 48% of nighttime chemistry OA observed by AMS,
49 respectively. Our PMF analysis also demonstrated that the highly oxygenated OA and
50 hydrocarbon-like OA cannot be identified with FIGAERO-CIMS in this study. In summary, our
51 results show that the volatility of OA is strongly governed by its formation pathways and subsequent
52 atmospheric aging processes.

53

54 **1. Introduction**

55 Secondary organic aerosols (SOA), a major component of fine particular matter (PM_{2.5}) in
56 China (Zhou et al., 2020), exert profound influences on climate change, human health, and air
57 quality (Arias et al., 2021; Apte et al., 2018; Huang et al., 2014). Despite notable reductions in
58 primary emission in recent years, SOA has emerged as an increasingly crucial factor in haze
59 formation in China (Zhang et al., 2018). However, accurately modeling SOA from current chemical
60 models is still challenging, largely attributed to our limited understanding of its formation
61 mechanisms (Charan et al., 2019; Matsui et al., 2009; Lu et al., 2020). Thus, there is a crucial need
62 for a comprehensive understanding of SOA formation and aging processes in the ambient
63 environment.

64 Positive matrix factorization (PMF) has been widely used to apportion the contribution of
65 primary and secondary sources to organic aerosol (OA) (Chen et al., 2014; Chen et al., 2021a; Ou
66 et al., 2023; Tian et al., 2016). For the input of OA, the matrix of time serial spectral of OA measured
67 by the Aerodyne Aerosol Mass Spectrometers (AMS) or Aerosol Chemical Speciation Monitor
68 (ACSM) was usually applied (Uchida et al., 2019; Canonaco et al., 2013). Based on this approach,
69 various primary OA (POA) components such as, hydrocarbon-like OA (HOA, associated with traffic
70 emission), biomass burning OA (BBOA), cooking OA (COA), and secondary OA (SOA) with
71 different oxidation levels are broadly identified in field measurements (Zhang et al., 2012; Jimenez
72 et al., 2009; Huang et al., 2010; Qin et al., 2017; Guo et al., 2020; Huang et al., 2018; Al-Naiema et
73 al., 2018). OA factors are generally distinguished according to their features on mass spectral and
74 time series (Ulbrich et al., 2009; Lee et al., 2015). However, the electric ionization sources (70ev),
75 together with thermal decomposition at 600C, lead to strongly fragmented ions detected in
76 AMS/ACSM. These fragmented ions lack parent molecular information, thus hindering the ability
77 to further attribute OA factors to more specific sources, thereby limiting our understanding of SOA
78 formation pathways and aging mechanisms in ambient environments. To overcome this challenge,
79 applying PMF analysis of molecular-level datasets is needed for refining SOA source apportionment.
80 Recently, chemical ionization mass spectrometer coupled with the Filter Inlet for Gases and
81 Aerosols (FIGAERO-CIMS) has been increasingly employed for the molecular-level
82 characterization of oxygenated organics compounds in the gas and particle phase (Ye et al., 2021;

83 Thornton et al., 2020). Using this approach, Ye et al. (2023) employed PMF analysis to FIGAERO-
84 CIMS data sets and found that low-NO-like pathway had a significant contribution to SOA
85 formation in urban area.

86 Volatility, an important property of organic compounds, is frequently described as saturation
87 mass concentration (C^* , Donahue et al., 2006). The volatility of organic compounds is closely
88 related to its chemical characteristics, including oxidate state, number of carbons, and functional
89 groups (Donahue et al., 2012; Donahue et al., 2011; Ren et al., 2022). The gas–particle partitioning
90 behavior of organic compounds is largely governed by their volatility, and thus strongly influence
91 the formation of SOA (Nie et al., 2022). Moreover, chemical processes occurring in the particle
92 phase can alter the volatility of organic compounds. For example, high molecular weight organic
93 compounds can form through accretion reactions, leading to a reduction in volatility (Barsanti and
94 Pankow, 2004; Jenkin, 2004; Kroll and Seinfeld, 2008). In addition, particle phase organic
95 compounds can be oxidized by atmospheric oxidants (e.g., O_3 , OH, and NO_3), which can also alter
96 the chemical characteristic and volatility (Rudich et al., 2007; Walser et al., 2007). Thus, the
97 variation of volatility can provide valuable information about the formation and aging processes of
98 OA. Graham et al. (2023) found that SOA from NO_3 oxidation of α -pinene or isoprene had a higher
99 volatility than it from β -caryophyllene. Hildebrandt Ruiz et al. (2015) demonstrated that exposure
100 to different OH levels could lead to a large variation in SOA volatility.

101 However, linking OA volatility directly to its chemical characteristics and sources remains
102 challenging. A thermodenuder (TD) coupled with an AMS has been employed to investigate the
103 volatility of OA from different sources (Louvaris et al., 2017). Xu et al. (2021) estimated the
104 volatility of different PMF OA factors in the North China Plain and reported that RH level could
105 alter both the formation pathway and volatility of more oxidized oxygenated OA. Feng et al. (2023)
106 reported the much lower OA volatility from out plumes of North China plain than results obtained
107 in the urban areas, signifying the aging impact on OA volatility. Nevertheless, owing to the
108 operational principle of AMS, it is still difficult to obtain molecular information of organic
109 compounds at different volatilities. In contrast, the FIGAERO-CIMS provides not only molecular-
110 level measurements but also thermal desorption profiles (thermograms) for each detected compound.
111 The temperature of the peak desorption signal (T_{max}) of a specific compound is typically correlated
112 with its volatility (Lopez-Hilfiker et al., 2014), enabling direct connects between the volatility and

113 organic molecular (Ren et al., 2022). Huang et al. (2019) analysis the ambient particles filter samples
114 collected in different seasons with FIGAERO-CIMS and reported a lower volatility of oxygenated
115 OA in winter, partly due to higher O:C. Buchholz et al. (2020) utilized PMF analysis of FIGAERO-
116 CIMS thermogram data sets to investigate physicochemical property of laboratory-generated SOA
117 particles.

118 To comprehensively investigate the evolution of OA and its relationship with volatility in
119 ambient environment, we employed a FIGAERO-CIMS along with other online instruments to gain
120 a comprehensive understanding of the variation in SOA volatility within urban plumes in the Pearl
121 River Delta (PRD) region during the fall of 2019. PMF analysis was performed on thermograms
122 data obtained from the FIGAERO-CIMS. By combining the source apportionment of thermogram
123 organic aerosol (OA) with corresponding volatility information, we investigated the potential
124 formation pathway and influencing factors of SOA in the urban downwind region.

125 **2. Measurement and Method**

126 **2.1 Field Measurements**

127 We conducted a field campaign at the Heshan supersite in the PRD region from September 29
128 to November 17, 2019. Considering the integrity of the measurements, we focus primarily on the
129 period from October 16 to November 16, 2019 in this study. The measurement site was located in a
130 rural area surrounded by farms and villages (at 22°42'39. 1"N, 112°55'35.9"E, with an altitude of
131 about 40 m), situated to the southwest of the PRD region. All online instruments were placed in air-
132 conditioned rooms on the top floor of the supersite building.

133 A FIGAERO-CIMS, coupled with an X-ray source, was used to measure organic compounds
134 in both the gas- and particle-phase, utilizing I⁻ as the chemical ionization reagent. The instrument
135 operated on one-hour cycle by switching between two modes (sampling mode and desorption mode)
136 for measuring gas- and particle-phase oxygenated organic molecules. In the sampling mode,
137 ambient gas was measured in the first 21 minutes, followed by a 3-min zero air background, while
138 the PM_{2.5} sample was collected on a PTFE membrane filter for 24 minutes. Then, the instrument
139 was switched to the desorption mode, in which the collected particles were desorbed using heated
140 N₂. The temperature of the N₂ was increased from approximately 25°C to 175°C over a 12-minute
141 period, and then held at 175°C for an additional 24 minutes. Calibration of a few chemicals was

142 conducted in the laboratory. For the remaining organic species, a voltage scanning method was used
143 to determine their sensitivities (referred to as semi-quantified species) (Ye et al., 2021; Iyer et al.,
144 2016; Lopez-Hilfiker et al., 2016). The detailed operation settings, data processing, and calibration
145 can be found in Cai et al. (2023) and Ye et al. (2021).

146 A soot particle aerosol mass spectrometer (SP-AMS, Aerodyne Research, Inc., USA) was used
147 to measure the chemical composition of PM₁ particles, including nitrate, sulfate, ammonium,
148 chloride, black carbon, and OA. More details on the quantification using ionization efficiency,
149 composition dependent collection efficiency, data analysis, and source apportionment of OA from
150 AMS data (defined as AMS-OA) could be found in Kuang et al. (2021) and Cai et al. (2024). In
151 brief, AMS-OA consisted of two primary OA factors and four secondary OA factors. The primary
152 OA factors include hydrocarbon-like OA (HOA, 11%) and biomass burning OA (BBOA, 20%),
153 which were mainly contributed by traffic and cooking emissions and biomass burning combustion,
154 respectively. For SOA factors, biomass burning SOA (BBSOA, 17%) was likely formed through
155 oxidation of biomass burning emission; less oxidized oxygenated OA (LO-OOA, 24%), which
156 results from strong daytime photochemical processes; more oxidized oxygenated OA (MO-OOA,
157 17%), related to regional transport; and nighttime-formed OA (Night-OA, 11%) which was
158 associated with nighttime chemistry.

159 Trace gases such as O₃ and NO_x were measured by gas analyzers (model 49i and 42i, Thermo
160 Scientific, US). Meteorological parameters, including wind speed and wind direction, were
161 measured by a weather station (Vantage Pro 2, Davis Instruments Co., US).

162 2.2 Methodology

163 Positive matrix factorization (PMF) is a widely used tool for source apportionment of long
164 timeseries data (Paatero and Tapper, 1994). In the desorption mode, the particulate organic
165 compounds are thermo-desorbed and simultaneously measured by the FIGAERO-CIMS. Organic
166 molecules with different volatility were characterized by thermograms (desorption signals vs
167 temperature of N₂). Here, we performed PMF analysis to the thermogram data of organic
168 compounds measured by the FIGAERO-CIMS (FIGAERO-OA) using the Igor-based PMF
169 Evaluation Tool (PET, v3.01, Ulbrich et al., 2009), which can be expressed as follows:

$$170 \quad \mathbf{X} = \mathbf{G}\mathbf{F} + \mathbf{E} \quad (1)$$

171 where \mathbf{X} is the thermogram organic compound data measured by the FIGAERO-CIMS. which

172 can be decomposed into two matrices \mathbf{G} and \mathbf{F} . The matrix \mathbf{G} , \mathbf{F} , and \mathbf{E} contain the factor time series,
173 factor mass spectra, and the residuals between the measured data and the reconstructed data.

174 The raw normalized count per second (NCPS) thermogram data with a time resolution of 1s
175 was averaged to a 20s-time grid, and then was background-corrected by subtracting linearly
176 interpolated background thermogram signals. For each scan, only the data points when the
177 desorption temperature increased were used as input data (corresponding to 25°C to 170 °C, 1-70
178 data points in this study, Fig. S1), since the main information lies during the species desorbing from
179 the FIGAERO filter (Fig. S1, Buchholz et al., 2020). Then, we combined data from separate
180 thermogram scans (without background scans) to a larger input data set.

181 To perform the PMF analysis, a data uncertainty matrix ($S_{i,j}$) is needed, where the i and j
182 represents the index of ions and data points, respectively. According to Buchholz et al. (2020), the
183 uncertainty was assumed to be constant for each individual thermogram scan (constant error
184 scheme). The $S_{i,j}$ of a specific thermogram scan can be determined by the following equation:

185
$$S_{i,j} = \sigma \quad (2)$$

186 For each thermogram scan, the last 20 data points are assumed to be in steady state. Thus, the
187 σ_{noise} was calculated as the median of the standard deviation of the residual ($res_{i,j}$), which can be
188 obtained from the difference between the data points ($Data_{i,j}$) and the corresponding linear fitted
189 value ($FittedData_{i,j}$) for the measured data points (Fig. S2):

190
$$res_{i,j} = Data_{i,j} - FittedData_{i,j} \quad (3)$$

191
$$\sigma = median(stdev(res_{i,j})) \quad (4)$$

192 Due to the large volume of the data matrix (59500×1028) exceeding the processing capacity
193 of the PET, we had to divide the data matrix into three parts and performed PMF analysis separately.
194 An eight-factor solution was selected for each part based on Q/Q_{exp} behavior and factor
195 interpretability (Fig. S3 to S6). To assess factor consistency, the mass spectra of resolved factors
196 were compared across different parts, showing strong correlations ($R>0.9$) for the each factor (Fig.
197 S7 and S8). Weaker correlations during the early campaign period (2 to 5 October) likely reflect
198 changes in dominant OA sources under different meteorological conditions (Fig. S8 and S9). After
199 excluding this period, consistent factor profiles were obtained and combined for further analysis.
200 Detailed evaluations are provided in the Section S1.

201 Since input data sets of PMF analysis were the NCPS data, the signal of each thermograms

202 factor was a combination of NCPS values of different ions. Thus, it is necessary to convert the signal
203 of these factors into mass concentrations, which would increase the representativeness of the
204 thermogram PMF results. The NCPS of a specific ion was linearly correlated with the corresponding
205 mass concentration. Thus, for a signal running cycle (a thermogram scan), the mass concentration
206 of a specific thermograms OA factor k (M_k) can be estimated as:

$$207 \quad M_k = \sum_i \left(\frac{\sum_j Signal_{j,k} \cdot Profile_{i,k}}{\sum_j NCPS_{j,i}} \cdot m_i \right) \quad (5)$$

208 where i and j represent the index of species and data points; the $Signal_{j,k}$ is the signal of a
209 thermograms OA factor k at a data index j ; the $Profile_{i,k}$ represents the fraction of signal of factor
210 k and ion i ; the $NCPS_{j,i}$ is the NCPS of species i at a data index j ; and m_i is the mass concentration
211 of species i in the particle-phase measured by the FIGAERO-CIMS.

212 For a specific organic compound, the temperature of the peak desorption signal (T_{max}) has a
213 nearly linear relationship with the logarithm of saturation vapor pressure (P_{sat}) of the respective
214 organic compound (Lopez-Hilfiker et al., 2014):

$$215 \quad \ln(P_{sat}) = aT_{max} + b \quad (6)$$

216 where a and b are fitting coefficients. P_{sat} can be converted to saturation vapor concentration
217 (C^* , $\mu\text{g m}^{-3}$) by following equation:

$$218 \quad C^* = \frac{P_{sat}M_w}{RT} 10^6 \quad (7)$$

219 where M_w is the average molecular weight of the organic compound (determined by the FIGAERO-
220 CIMS), R is the gas constant ($8.314 \text{ J mol}^{-1} \text{ K}^{-1}$), and T is the thermodynamic temperature (298.15
221 K). The fitting parameters of a and b were calibrated by a series of polyethylene glycol (PEG 5-8)
222 compounds before the campaign. PEG standards (dissolved in acetonitrile) were atomized using a
223 homemade atomizer, and the resulting particles were size-classified by a differential mobility
224 analyzer (DMA; model 3081L, TSI Inc.) to target diameters of 100 and 200 nm. The size-selected
225 particles were then split into two flows: one directed go to a CPC (3775, TSI) for the measurements
226 of number concentration, and the other to the FIGAERO-CIMS particle inlet. The collected mass
227 by CIMS was calculated based on the particle diameter, number concentration, FIGAERO-CIMS
228 inlet flow rate, and collection time. The details of the calibration experiments and selection of fitting
229 coefficients (a and b) can be found in table S1 and Cai et al. (2024). In this study, the fitting
230 parameters (a=-0.206 and b=3.732) were chosen, as the mass loading (407 ng) and diameter (200

231 nm) are closest to the ambient samples, since the collected mass loading centered at about 620 ng
232 and the particle volume size distribution (PVSD) centered at about 400 nm (Cai et al., 2024). It was
233 worth noting that the volatility range of PEG 5-8 ($-1.73 \leq \log_{10} C^* \leq 3.34 \mu\text{g m}^{-3}$) may not fully
234 represent the volatility of ambient organic aerosol, particularly nitrogen-containing and highly
235 oxygenated compounds that can exhibit much lower volatility ($\log_{10} C^* \leq -2 \mu\text{g m}^{-3}$, Ren et al., 2022;
236 Chen et al., 2024). At present, saturation vapor pressure data for PEG standards are only available
237 up to PEG-8 (Krieger et al., 2018). Ylisirniö et al. (2021) demonstrated that different extrapolation
238 approaches for estimating the volatility of higher-order PEGs can lead to substantial discrepancies
239 in calibration results, and they strongly recommended that higher-order PEGs should only be used
240 to extend the volatility calibration range once their saturation vapor pressures are accurately
241 determined. Very recently, Ylisirniö et al. (2025) derived saturation vapor pressures for higher-order
242 PEGs up to PEG-15 and demonstrated that extending FIGAERO-CIMS calibration to much lower
243 volatilities is feasible, but also showed that different estimation approaches for higher-order PEGs
244 can lead to large discrepancies, highlighting substantial uncertainties when extrapolating volatility
245 calibration beyond PEG-8. Therefore, uncertainties may remain in the calibration of low-volatility
246 OA, and further calibration experiments using complementary techniques are highly recommended.
247 Therefore, uncertainties may remain in the calibration of low-volatility OA, and further calibration
248 experiments using complementary techniques are highly recommended.

249 **3 Results**

250 **3.1 Overview of FIGAERO-OA factors**

251 In this study, the average mass concentration of FIGAERO-OA was about $5.3 \pm 2.4 \mu\text{g m}^{-3}$. The
252 thermogram data sets of FIGAERO-OA were analyzed with PMF and mass concentration of each
253 factor was estimated based on eq. (5), which provide volatility and mass concentration information
254 of OA originating from different formation pathways. An 8-factor solution was chosen to explain
255 the thermogram of FIGAERO-OA. These factors included six associated with daytime
256 photochemical reactions, one related to biomass-burning, and one factor contributed by nighttime
257 chemistry. The diurnal variation, mass spectra, and thermograms of these factors can be found in
258 Fig. S9. The estimated volatility ($\log_{10} C^*$), T_{max} , and elemental information of all factors are
259 shown in table 1. Given that the thermogram data can provide volatility information of organic

260 compounds, the identified OA factors were categorized based on their potential formation pathway,
261 volatility, and correlation with AMS PMF factors (Table 1 and Fig. S10). For example, if the PMF
262 factor with a T_{max} located in the ranges of low volatile organic compounds (LVOC, approximately
263 corresponding to 78.8 °C to 112.3 °C then Fig. 1), this factor will be named after low volatility OA
264 (LVOA). For the factors whose T_{max} is above 112.3 °C, extremely low volatility (ELVOA) will be
265 named.

266 The six daytime chemistry related factors include a low volatility OA factor likely formed
267 under high NO_x condition (Day- HNO_x -LVOA, 12%), a low volatility factor contributed by gas-
268 particle partitioning (Day- LNO_x -LVOA, , 11%), a low volatility and an extremely low volatility
269 factor originating from the daytime aging process (Day-aged-LVOA and Day-aged-ELVOA, 16%
270 and 11% respectively), and a low volatility and an extremely low volatility factors related to urban
271 air masses (Day-urban-LVOA and Day-urban-ELVOA, 16% and 7%, respectively). These daytime
272 factors accounted for about 76.4% of the total mass of FIGAERO-OA and demonstrated distinct
273 daytime peak. The total mass of daytime FIGAERO-OA factors showed a strong positive correlation
274 with LO-OOA in AMS-OA ($R=0.86$), which was attributed to photochemical reactions (Fig. S10a).

275 Both Day- HNO_x -LVOA and Day- LNO_x -LVOA reached their peak values at about 14:00 LT
276 (Fig. 1 a1 and b1), implying strong photochemical production. Day- HNO_x -LVOA had the highest
277 N:C (0.06) and the lowest oxidation state ($\overline{OS_c}=-0.01$), which could be attributed to the “high NO_x ”
278 formation pathway. It was also supported by significant positive correlation ($R=0.93-0.94$) with
279 particulate phase nitrogen-containing organic compounds (e.g., $\text{C}_4\text{H}_5\text{NO}_6$, $\text{C}_8\text{H}_{11}\text{NO}_8$, and
280 $\text{C}_8\text{H}_{11}\text{NO}_9$). Previous studies found that high NO_x concentration can suppress the production of
281 molecules with a high oxidation degree (Rissanen, 2018; Praske et al., 2018), which could explain
282 the low $\overline{OS_c}$ value (-0.01) and relative high volatility ($\log_{10} \overline{C^*}=-0.98$) found for Day- HNO_x -LVOA.
283 Day- LNO_x -LVOA had a higher $\overline{OS_c}$ (0.18) and lower $\log_{10} \overline{C^*}$ (-2.71) than Day- HNO_x -LVOA,
284 consistent with that Day- LNO_x -LVOA was composed of smaller and more oxidized non-nitrogen
285 containing compounds (e.g., $\text{C}_2\text{H}_2\text{O}_3$, $\text{C}_3\text{H}_4\text{O}_3$, $\text{C}_4\text{H}_6\text{O}_4$, and $\text{C}_6\text{H}_8\text{O}_4$). Noting that C2-C3 group
286 could originate from the decomposition of larger molecules during thermal desorption, since the
287 thermogram of $\text{C}_2\text{H}_2\text{O}_3$ and $\text{C}_3\text{H}_4\text{O}_3$ demonstrated a bimodal distribution (Fig. 9 a). Figure S12 b
288 and d further examine the contribution of all FIGAERO factors to the signals of $\text{C}_2\text{H}_2\text{O}_3$ and $\text{C}_3\text{H}_4\text{O}_3$.
289 One mode, peaking in the LVOC range, was primarily associated with Day- LNO_x -LVOA, and a

290 second mode, peaking in the ELVOC range, was dominated by Day-aged-ELVOA. These results
291 indicates that these two low molecular weight species are likely decomposition products of at least
292 two distinct classes of higher molecular weight organic compounds.

293 Additionally, we identified two aged OA factors (Day-aged-LVOA and Day-aged-ELVOA)
294 with an afternoon peak at about 18:00 LT (Fig. 1 c1 and d1), which may be derived from the aging
295 transformation of preexisting organic aerosols via daytime photochemical reactions. These aged
296 factors exhibited the highest $\overline{OS_c}$ (0.35 and 0.40) and relatively low volatility with a $\log_{10} \overline{C^*}$ of -
297 2.02 and -4.80, respectively. Day-aged-LVOA was featured with a series of C₄-C₈ oxygenated
298 compounds (e.g., C₄H₆O₅, C₅H₈O₅, C₆H₁₀O₅, C₇H₁₀O₅, and C₈H₁₂O₅). In contrast, Day-aged-
299 ELVOA had a higher fraction of smaller molecules (e.g., C₂H₄O₃ and C₃H₆O₃, Fig. 1d2). Chen et
300 al. (2021b) found that low molecular weight carboxylic acids (LMWCA) could form through SOA
301 aging processes and report a strong correlation ($R^2=0.90$) between LMWCA and highly oxygenated
302 OA. However, C₂H₄O₃ and C₃H₆O₃ had a weak correlation ($R=0.49$ and 0.13) with MO-OOA
303 resolved from AMS (Fig. S11). In addition, the T_{max} of C₂H₄O₃ and C₃H₆O₃ located in the ELVOC
304 range and showed thermogram profiles similar to that of Day-aged-ELVOA (Fig. S12a). The
305 thermogram signal of C₂H₄O₃ and C₃H₆O₃ was mainly contributed by Day-aged-ELVOA (Fig. S12
306 c and e), supporting the interpretation that these species are more likely decomposition products of
307 low volatility organic compounds rather than being directly formed through atmospheric aging
308 processes.

309 Two urban air masses-related OA factors (Day-urban-LVOA and Day-urban-ELVOA) were
310 identified, which would be discussed in the following section. Day-urban-LVOA demonstrated
311 comparable $\overline{OS_c}$ (0.08), O:C (0.80) and volatility (-0.90) to Day-HNO_x-LVOA (-0.01, 0.75, and -
312 0.98, respectively), but show a higher fraction of non-N-containing molecules (e.g., C₄H₆O₄,
313 C₅H₆O₄, C₅H₈O₅, and C₇H₁₀O₅) and a reduced N:C ratio (Table 1). However, the oxidation state
314 ($\overline{OS_c}$) of Day-HNO_x-LVOA (-0.01) was significantly lower than that of Urban-LVOA (0.08) ,
315 accompanied by a relatively higher N:C (0.06 vs 0.04). Despite its lower oxidation state, the
316 volatility of Day-HNO_x-LVOA is comparable to that of Day-urban-LVOA, which may reflect
317 differences in functional group composition. For example, a nitrate group (-ONO₂) contributes to
318 volatility reduction at a level comparable to that of a hydroxyl group (-OH) and generally more
319 strongly than carbonyl functionalities such as aldehydes (-C(O)H) or ketones (-C(O)-) (Pankow

320 and Asher, 2008). However, due to instrumental limitations, we are unable to directly resolve the
321 functional group composition of individual OA factors, and further measurements employing new
322 techniques are needed to better constrain the role of functional groups in controlling the volatility
323 of ambient organic aerosol. Day-urban-ELVOA had the lowest volatility ($\log_{10} C^* = -7.18$) but an
324 $\overline{OS_c}$ (0.27) lower than Day-aged-ELVOA (0.34) and composed of oxygenated compounds (e.g.,
325 $C_8H_{10}O_5$, $C_7H_8O_5$, $C_6H_8O_4$, and $C_5H_6O_4$). The thermogram of Day-aged-ELVOA demonstrates
326 bimodal distribution (peaked at LVOC and ELVOC range) and had a highest T_{max} (153.2 °C)
327 among thermograms OA factors (Fig. 1f3). However, the majority of organic molecules (e.g.,
328 $C_5H_6O_4$, $C_4H_6O_5$, $C_6H_8O_4$, and $C_8H_{10}O_5$) do not exhibit thermograms similar to that of Day-urban-
329 ELVOA (Fig. S13). Instead, their thermograms demonstrate multimodal distributions and are
330 contributed by multiple FIGAERO factors. For example, a mode of $C_5H_6O_4$ peaking in the LVOC
331 range was mainly contributed by Day-urban-LVOA, while two modes peaking in the ELVOC range
332 were primarily contributed by Day-aged-ELVOA and Day-urban-ELVOA, respectively. These
333 results suggest that these molecules may originate from both direct desorption of organic aerosol
334 and thermal decomposition of higher-molecular-weight compounds during heating.

335 The biomass-burning related factor, biomass-burning less volatile organic aerosol (BB-LVOA,
336 10% of FIGAERO-OA), had a low $\overline{OS_c}$ (-0.07), the lowest O:C (0.74), and positive correlation with
337 BBOA resolved from AMS ($R=0.64$, Fig. S10b). It presented a prominent peak at 19:00 LT and was
338 identified by the distinctive tracer levoglucosan ($C_6H_{10}O_5$), nitrocatechol ($C_6H_5NO_4$), and
339 nitrophenol ($C_6H_5NO_3$, Fig. 1) in the spectrum, which was frequently detected in biomass burning
340 plumes (Gaston et al., 2016; Ye et al., 2021). In the upwind urban region of Heshan site, Ye et al.
341 (2023) identified a biomass burning related factor in Guangzhou city using the FIGAERO-CIMS,
342 with a distinct evening peak at 21:00 LT and more abundance oxygenated compounds (e.g., $C_7H_{10}O_5$
343 and $C_8H_{12}O_6$). The different oxidation level of BBOA between Guangzhou and Heshan, suggest the
344 BB-LVOA in this study is more related to the direct BB emission, but the BB factor in Guangzhou
345 is more resembled BB related SOA factor. This statement was supported by the fact that biomass
346 burning activities were frequently observed near the measurement site during this study, while the
347 biomass burning activities in urban areas was prohibited and can be transported from nearby
348 suburban agricultural areas (Cai et al. 2023) .

349 The nighttime chemistry related less volatile OA (Night-OA, 15% of FIGAERO-OA) has the
350 highest N:C (0.07) and exhibited an enhanced at nighttime (22:00-24:00 LT, Fig. 1). Notably, this
351 nighttime factor was composed of a series of organic nitrates (e.g., $C_8H_{11}NO_7$, and $C_{10}H_{15}NO_7$),
352 which was related to the products from monoterpenes oxidized by the NO_3 radical or oxidation of
353 biomass burning products during nighttime (Faxon et al., 2018; Decker et al., 2019). Noting that the
354 levoglucosan ($C_6H_{10}O_5$) was also abundant in the Night-LVOA, suggesting that part of this factor
355 could be attributed to the nighttime aging process of biomass burning products (Jorga et al., 2021).
356 The detailed discussion about the potential formation pathway of these six daytime FIGAERO-OA
357 factors will be discussed in section 3.2.

358 The volatility of organic compounds was closely related to their chemical characteristics
359 (Donahue et al., 2012). Figure 2 demonstrates the relationship between $\log_{10} \overline{C^*}$ of thermogram
360 factors and $\overline{OS_c}$, O:C, and number of carbons (nC). In general, these factors exhibited a negative
361 correlation ($R=-0.60$ and -0.73) with both the $\overline{OS_c}$ and the O:C but showed a positive correlation
362 ($R=0.73$) with nC (Fig. 2), except for Day-urban-ELVOA. As aforementioned, the major component
363 of Day-urban-ELVOA could be decomposition products of larger oxygenated molecules. Thus, the
364 chemical characteristic of Day-urban-ELVOA did not demonstrate a similar relationship of volatility
365 versus molecule indicators (e.g., oxidation state, O:C and nC) as other factors. The increase of
366 carbon number usually lead to a decrease in volatility (Donahue et al., 2011), while this trend
367 overturned in this campaign (Fig. 2c). Fig. 2d shows that $\overline{OS_c}$ had a negative relationship ($R=-0.84$)
368 with carbon number, suggesting that organic factors with a higher oxidation degree had a shorted
369 carbon backbone. It could be partly owing to fragmentation of organic molecules during aging
370 processes (Chacon-Madrid and Donahue, 2011; Jimenez et al., 2009). Consistently, two aged factors
371 (Day-aged-LVOA and Day-aged-ELVOA) had a higher $\overline{OS_c}$ and a lower carbon number than other
372 factors. Additionally, it indicates that the increase in oxidation degree outweighed the effect of
373 decreasing nC , leading to a reduction in the volatility of OA during this campaign.

374 The temporal variation of volatility distribution and mean C^* of FIGAERO-OA, the sum of
375 six daytime factors in FIGAERO-OA and LOOA in AMS OA, mass fraction of eight FIGAERO-
376 OA factors, and wind direction and speed are demonstrated in Fig. 3. As shown in Fig. 3, the
377 increase of mean C^* during the daytime (6:00 LT to 18:00 LT, Fig. S14 a) is usually accompanied
378 by the enhancement of daytime factors in FIGAERO-OA and LO-OOA from AMS (Fig. S14 b and

379 c), indicating that the formation of these factors could notably increase OA volatility. Notably,
380 FIGAERO-OA with a $\log_{10} C^*$ of $-1 \mu\text{g m}^{-3}$ showed pronounced enhancements during the
381 increasing of mean C^* , implying that the volatility of six daytime factors might cluster around 10^{-1}
382 $\mu\text{g m}^{-3}$ (Fig. S14d). In Fig. 3b, distinct diurnal variation of O_x ($\text{O}_x=\text{O}_3+\text{NO}_2$) was observed during
383 the campaign. The maximum of O_x can be as high as $230 \mu\text{g m}^{-3}$, highlighting strong photochemical
384 reaction. The daytime factors, especially Day- HNO_x -LVOA (Fig. 3c), exhibited markable
385 enhancements under weak northwesterly to northeasterly wind (Fig. 3d and Fig. S15). A backward
386 trajectory analysis revealed that the measurement site was mainly affected by the urban pollutants
387 from the city cluster around Guangzhou (Fig. S16). Two periods, which were long-range transport
388 and urban air massed periods, respectively, were selected to further analyze the impact of urban
389 pollutants on the formation and aging process of OA. The variation of OA volatility based on wind
390 direction and speed, together with backward trajectory analysis, were also explored (Fig. S16 and
391 Table S2). In general, during the urban air masses period, the site was influenced by regional urban
392 plumes from the northeast city cluster, while the long-range transport period was primarily
393 associated with air masses advected from the northeast inland regions. More detailed discussion will
394 be shown in the following section.

395 **3.2 Potential formation pathway of FIGAERO-OA**

396 Figure 4 demonstrates distinct differences in the diurnal variation of thermograms factors
397 (including Day- HNO_x -LVOA, Day-aged-LVOA, Day-urban-LVOA, and Day-urban-ELVOA)
398 during long-range transport period and urban air masses period. During the urban air masses period,
399 Day- HNO_x -LVOA significantly increased from $\sim 0.4 \mu\text{g m}^{-3}$ to $\sim 4.8 \mu\text{g m}^{-3}$ in the daytime. The mass
400 concentration of Day-urban-LVOA and Day-urban-ELVOA demonstrated daytime enhancements
401 only during urban period, suggesting that the formation of these factors was closely related to the
402 pollutants in the urban plumes. Consistently, During the urban air masses period, the maximum
403 ozone concentration in the afternoon (12:00-18:00 LT, $208.3 \mu\text{g m}^{-3}$) was higher than that (185.5
404 $\mu\text{g m}^{-3}$) during long-range transport period, indicating a stronger photochemical reaction in the urban
405 plumes (Fig. 4). Thus, the daytime thermogram factors accounted for a higher fraction (79% vs 75%)
406 of FIGAERO-OA (Fig. S17). Additionally, the average mass concentration of all thermogram
407 factors ($8.9 \pm 5.1 \mu\text{g m}^{-3}$) was noticeably increased compared to the long-range period ($5.3 \pm 2.4 \mu\text{g}$
408 m^{-3}). Elevated NO_x concentration was observed in the urban plumes in the afternoon (12:00 LT-

409 18:00 LT, 17.4 ppbv vs 11.7 ppbv), which might also affect the formation pathway of SOA. Both
410 NO and NO/NO₂ remained at a relative low level (0.6-0.8 ppbv and <0.5) in the afternoon during
411 these two periods (Fig. S18), suggesting an important role of low-NO-like pathway (Ye et al., 2023).
412 Nihill et al. (2021) found that the production of OH and oxidized organic molecules would be
413 suppressed under high NO/NO₂ (>1) condition. Notably, Day-HNO_x-LVOA accounted for the
414 largest portion (29%) of FIGAERO-OA in the afternoon (12:00-18:00 LT, Fig. S19), followed by
415 Day-aged-LVOA (21%), while Day-LNO_x-LVOA contributed only 6%. In contrast, during the
416 long-range transport period, the mass fraction of Day-LNO_x-LVOA significantly increased (from
417 6% to 15%) along with a decrease in Day-HNO_x-LVOA (from 29% to 21%). These results indicate
418 that elevated NO_x concentration in urban plumes might alter the formation pathway of SOA (Cai et
419 al., 2024). Note that the sum of six daytime FIGAERO factors showed a positive relationship
420 (R=0.80 and 0.76, respectively) with LOOA during both periods (Fig. S20). However, the slope
421 (0.81) of the linear regression during the urban air masses period was higher than that (0.58) during
422 the long-range transport period, indicating that a higher fraction of LOOA could be detected by the
423 FIGAERO-CIMS during urban air masses period. This difference could be related to the
424 discrepancy in OA volatility. According to Cai et al. (2024), the volatility of OA was higher during
425 the urban air masses period.

426 To explore the potential formation pathway of daytime factors, figure 5 demonstrates the
427 variation of mass concentrations of six daytime factors as a function of O_x, total gas-phase organic
428 molecules measured by the FIGAERO-CIMS (referred as organic vapors), and NO₃⁻/SIA. Five
429 factors, excluding Day-urban-LVOA, exhibited positive correlations with O_x, highlighting the
430 critical role of photochemical reactions in their formation. Previous studies have demonstrated that
431 gas-particle partitioning plays a key role in SOA formation (Nie et al., 2022; Wang et al., 2022). In
432 this study, organic vapors had strong positive correlations with Day-HNO_x-LVOA (R=0.73) and
433 Day-LNO_x-LVOA (R=0.74), suggesting that these factors were mainly formed via gas-particle
434 partitioning. The median concentration of Day-HNO_x-LVOA dramatically increased (from ~0 to
435 ~5.6 $\mu\text{g m}^{-3}$) with rising organic vapors, whereas a comparable enhancement was not observed for
436 Day-LNO_x-LVOA (Fig. 5 b1 and b2).

437 Furthermore, NO_x impact on Day-HNO_x-LVOA and Day-HNO_x-LVOA was investigated here.
438 Fig. S21 show Day-HNO_x-LVOA concentrations were consistently higher under elevated NO_x

439 conditions, while Day-HNO_x-LVOA decreased with increasing NO_x level. Figure 6a displays the
440 mass ratio of Day-HNO_x-LVOA to Day-LNO_x-LVOA obviously increased with organic vapors (up
441 to 12~26) under high NO_x condition (>20 ppbv), while the ratio remained at approximately 2 at
442 low NO_x level (<10 ppbv). These overall results suggest that Day-HNO_x-LVOA formation was
443 predominantly governed by gas-particle partitioning under high NO_x condition, which were
444 typically sustained during urban air masses period (Fig. 2d). Figure 6b compares the relative mass
445 fraction of molecular composition in two gas-particle partitioning related factors, Day-HNO_x-
446 LVOA and Day-LNO_x-LVOA. The mass fraction of species was derived from the signal profile of
447 corresponding factors based on their sensitivity (Ye et al., 2021). Day-HNO_x-LVOA presented
448 greater proportions (10⁻⁵~10⁻³) of organic nitrates (ONs) than Day-LNO_x-LVOA (10⁻¹¹~10⁻⁹),
449 including C₄H₇NO₆, C₈H₉NO₄, C₈H₁₁NO₇, as well as nitrophenols (e.g., C₇H₇NO₃), which are
450 characterized by relatively low \overline{OS}_C . These compounds were probably attributed to the SOA
451 formation under elevated NO_x concentration (Fig. 2d). In contrast, Day-LNO_x-LVOA was enriched
452 in non-nitrogen-containing species (e.g., C₄H₆O₃, C₅H₁₀O₃, C₁₁H₁₇O₆), which exhibited a higher
453 \overline{OS}_C . These results indicate that NO_x exerts contrasting effects on the formation of these two gas-
454 particle partitioning-related factors.

455 Previous studies show that NO_x has a nonlinear effect on the formation of highly oxygenated
456 organic (HOM) compounds by influencing the atmospheric oxidation capacity and RO₂
457 autoxidation (Xu et al., 2025; Pye et al., 2019; Shrivastava et al., 2019). NO_x could suppress the
458 production of low-volatility molecules by inhibiting autoxidation (Rissanen, 2018; Praske et al.,
459 2018), while Nie et al. (2023) found that NO could enhance the formation of HOM at low NO
460 condition (< 82 pptv). During this campaign, the average NO_x and NO was about 24.0 ppbv and 2.3
461 ppbv, respectively, substantially higher than the “low-NO-regime” described by Nie et al. (2023).
462 Our previous study reported a lower concentration of organic vapors with a high \overline{OS}_C within urban
463 plumes during the same campaign (Cai et al., 2024). We investigate diurnal evolution of organic
464 compositions under long-range transport and urban air masses periods (Fig. S22). Mass
465 concentrations of CHON increase during the daytime in both periods, with a more pronounced
466 enhancement observed in urban air masses (Fig. S22a). However, the mass fraction of CHON was
467 lower during the urban air masses period than during the long-range transport period. We speculated
468 that elevated NO_x enhances overall oxidation and product formation rather than selectively

enriching nitrogen-containing compounds. This interpretation is consistent with results from our previous observation-constrained box-model simulations, in which production rates of OH and organic peroxy radicals (RO_2) were evaluated under varying NO_x and VOC conditions (Cai et al., 2024). The modeled $P(\text{OH})$ were close to the transition regime, indicating that elevated NO_x can enhance atmospheric oxidation capacity. In contrast, the $P(\text{RO}_2)$ was in the VOC-limited regime and decreased with increasing NO_x . Consistent with these results, Fig. S22c shows that the mass fraction of highly oxygenated organic molecules ($\text{O} \geq 6$) is lower during urban air masses period. Concurrently, species with low oxygen numbers ($\text{O} \leq 3$) become relatively more abundant in the urban plumes (Fig. S22c), indicating a shift in the oxidation product distribution toward less oxygenated and potentially more volatile compounds, the NO_x -driven suppression of multigenerational autoxidation inferred from the box-model results. This suppression of oxidation is observed for both CHON and CHO species. The average O:C of CHON (Fig. S22b) and CHO (Fig. S22e) are both lower during the urban air masses period, suggesting that enhanced NO_x broadly suppresses autoxidation across organic compound classes.

Furthermore, as illustrated in Fig. S23, the mass concentration of SVOC ($-0.5 < \log_{10} C^* < 2.5 \mu\text{g m}^{-3}$) and LVOC ($-3.5 < \log_{10} C^* < -0.5 \mu\text{g m}^{-3}$, Donahue et al., 2012) in the gas phase exhibited an increase ($2.5 \mu\text{g m}^{-3}$ at $\text{NO}_x < 10 \text{ ppbv}$ vs $3.3 \mu\text{g m}^{-3}$ at $\text{NO}_x \geq 30 \text{ ppbv}$) with the increase in NO_x , suggesting that these species likely contributed to the formation of Day- HNO_x -LVOA. Xu et al. (2014) found that both SOA volatility and oxidation state exhibited a nonlinear response to NO_x in a series of chamber environment. SOA volatility decreases with increasing NO_x level when the ratio of initial NO to isoprene was lower than 3. At higher NO_x level, higher volatile SOA was produced, probably owing to the more competitive $\text{RO}_2 + \text{NO}$ pathway. Figure 5 c1 and c2 investigate the relationship between these two factors and NO_3^-/SIA . Day- HNO_x -LVOA had a weak correlation ($R=0.30$) with NO_3^-/SIA , while this trend overturned ($R=-0.35$) for Day- LNO_x -LVOA. Yang et al. (2022) showed that $\text{OH} + \text{NO}_2$ pathway mainly contribute to the formation of nitrate in this campaign. Together, these results indicate that elevated NO_x suppressed the formation of highly oxygenated organic compounds, thereby limiting the contribution to Day- LNO_x -LVOA. Thus, the Day- LNO_x -LVOA was more likely formed via gas-particle partitioning under relatively low NO_x condition.

It is worth noting that $\text{C}_4\text{H}_7\text{NO}_5$, likely originating from isoprene photooxidation in the presence of NO_x (Fisher et al., 2016; Paulot et al., 2009), also show a higher fraction in Day- LNO_x -

499 LVOA (9.36×10^{-5} vs 4.93×10^{-11} in Day-HNOx-LVOA). A plausible explanation is that Heshan site,
500 located at a suburban region, experienced ambient NO_x levels (~ 13 ppb in the afternoon) sufficient
501 to facilitate the formation of $\text{C}_4\text{H}_7\text{NO}_5$. It is further supported by the observation that both particle-
502 and gas-phase $\text{C}_4\text{H}_7\text{NO}_5$ showed no significant variation with increasing NO_x (Fig. S24).

503 For the two urban-related factors, a positive correlation with O_x was observed only during the
504 urban air masses period ($R=0.46$ and 0.64 vs -0.05 and 0.28 in the long-range transport period, Fig.
505 20 a and c). Notably, Day-urban-LVOA increased from ~ 1.0 to $\sim 2.6 \mu\text{g m}^{-3}$ as O_x rose from 75 to
506 $275 \mu\text{g m}^{-3}$ during this period, while it remained relatively stable ($\sim 0.4 \mu\text{g m}^{-3}$) during the long-
507 range transport period (Fig. S25). In addition, Day-urban-LVOA showed only a limited similarity
508 in its variation trend to Day-HNOx-LVOA during the urban air mass period (Fig. S26). This finding
509 supports the hypothesis that the daytime formation of urban-related OA factors was closely related
510 to the urban pollutants. Additionally, Day-urban-ELVOA exhibited a positive correlation with
511 organic vapors ($R = 0.65$, Fig. S25b), while such a correlation was not observed for Day-urban-
512 LVOA. It implies that Day-urban-ELVOA may primarily form through gas-particle partitioning
513 during the urban air mass period.

514 Day-urban-LVOA was also positively correlated with NO_3^-/SIA (Fig. 5c), consistent with the
515 concurrent enhancement of nitrate and SOA during haze episodes (Ye et al., 2023; Zheng et al.,
516 2021). During the urban air masses period, nitrate demonstrates a bimodal diurnal variation with
517 peaks in both the morning and afternoon (Fig. S27), the latter peak likely attributed to $\text{OH}+\text{NO}_2$
518 pathway (Yang et al., 2022). Day-urban-LVOA had a significant correlation ($R=0.97$) with
519 succinic acid ($\text{C}_4\text{H}_6\text{O}_4$) in the particle phase (Fig. S28), which was previously reported to form via
520 multiphase reaction during haze episode in megacity (Zhao et al., 2018; Zheng et al., 2021). As
521 shown in Fig. S29, Day-urban-LVOA also increased with the ratio of the aerosol liquid water
522 content (ALWC) to PM_1 , further indicating that aqueous processes in urban plumes played an
523 important role in its enhancement.

524 For the aging factors, Day-aged-LVOA and Day-aged-ELVOA exhibited peak concentrations
525 about 3 hours later (at about 18:00 LT, Fig. 4) than other day factors (15:00 LT). It suggests that the
526 two aged factors might originate from the photochemical aging processes of preexisting organic
527 aerosols. To further explore the formation and aging process of these daytime factors, we estimated
528 their daytime enhancement (Δ). For factors peaked at 15:00 LT, the Δ was estimated as the difference

529 between the average mass concentration during 00:00-6:00 LT and 12:00-18:00 LT. For factors
530 peaking at about 18:00 LT, Δ was regarded as the difference between the average mass
531 concentration during 6:00-12:00 LT and 15:00-21:00 LT, since these factors remained at a relatively
532 high-level during nighttime probably owing to lower boundary layer height. The Δ Day-aged-
533 LVOA showed strong positive correlations with Δ Day-HNO_x-LVOA ($R=0.73$), Δ Day-urban-
534 LVOA ($R=0.77$), and Δ Day-LNO_x-LVOA ($R=0.64$, Fig. 7a), suggesting that its formation might
535 be closely associated with the aging processes of these three factors. Similarly, Δ Day-aged-ELVOA
536 was positively correlated with both Δ Day-LNO_x-LVOA ($R=0.61$), Δ Day-urban-LVOA ($R=0.67$),
537 and Δ Day-urban-ELVOA ($R=0.73$, Fig. 7c). In contrast, we did not observe such correlations
538 between Δ Day-aged-ELVOA and Δ Day-HNO_x-LVOA ($R=0.49$, Fig. 7c). It implies that the
539 formation of Day-aged-ELVOA was likely more influenced by the aging of urban-related factors
540 and Day-LNO_x-LVOA.

541 3.3 Comparison with AMS OA

542 Adopting PMF analysis to thermogram datasets provides valuable insights into the formation
543 and aging processes of SOA. However, the representativeness of FIGAERO-OA still requires
544 evaluation. Figure 8 compares FIGAERO-OA with AMS-OA during two different periods. In
545 general, FIGAERO-OA could not explain MO-OOA and HOA identified in AMS OA, given that
546 all thermogram factors had a weak correlation ($R=-0.18$ – 0.36) between these two factors (Table S2).
547 MO-OOA, which had the highest O:C (1.0) among all AMS factors (0.32–1.0) (Cai et al., 2024),
548 was likely low volatile, meaning that much of this fraction might not have been vaporized during
549 the heating process. Xu et al. (2019) investigate the volatility of different OA factors using the
550 TD+AMS method and found that MO-OOA evaporated ~52% at $T=175^{\circ}\text{C}$. Another TD+AMS field
551 study in the North China Plain suggested that the volatility of MO-OOA varied with RH levels,
552 more MO-OOA evaporate at higher RH levels ($\text{RH}>70$, Xu et al., 2021), suggesting that MO-OOA
553 compounds formed at high RH condition could be higher volatile. During this campaign, the RH
554 varied from 25% to 92% which likely caused variability in MO-OOA volatility and thus in the
555 fraction desorbed at 175°C . This variability might explain the low correlation between MO-OOA
556 in AMS and all FIGAERO-OA factors. HOA mainly consists of hydrocarbon-like organic
557 compounds, which could not be detected by the FIGAERO-CIMS. The iodide source of the
558 FIGAREO-CIMS is selective towards multi-functional organic compounds (Lee et al., 2014),

559 making it less sensitive to detection hydrocarbon-like species. Ye et al. (2023) preformed
560 factorization analysis of data obtained from the FIGAERO-CIMS and AMS and suggested that
561 FIGAERGAERO-CIMS and AMS and suggested that FIGAERO-derived OA factors could not
562 account for all primary OA components resolved by AMS, including COA, NOA, and HOA. These
563 findings highlight the need for further investigations into the chemical characteristics of primary
564 OA to better understand their emission signatures and atmospheric evolution.

565 BBSOA in AMS-OA had a bimodal diurnal distribution with an afternoon peak ($\sim 14:00$ LT)
566 and an evening peak ($\sim 17:00$ LT, Fig. S30). The enhancement was more pronounced in the
567 afternoon (~ 1.6 to $\sim 3.6 \mu\text{g m}^{-3}$) compared to the evening (~ 2.9 to $\sim 4.0 \mu\text{g m}^{-3}$). Thus, we classify
568 both BBSOA and LOOA as daytime SOA. Six thermogram daytime factors could explain the
569 majority (82% on average) of daytime SOA with the explained fraction increasing from 78% during
570 the long-range transport period to 85% during the urban air masses period (Fig. 8 a and b). In both
571 periods, the summed thermogram daytime factors exhibited a diurnal variation like that of
572 LOOA+BBSOA (Fig. 8 c and d). Thermogram daytime OA was close to AMS daytime OA in the
573 morning but fell below AMS OA afternoon. The discrepancy in the afternoon could be related to
574 the decrease in OA volatility through strong photochemical reactions. Since the heating temperature
575 of the FIGAERO-CIMS was set at 175°C , compounds of very low volatility might not have been
576 fully detected. This discrepancy narrowed during the urban air masses, likely owing to the strong
577 SOA formation through gas-particle partitioning, which increased OA volatility (Cai et al., 2024).
578 The gap persisted overnight, owing to suppressed vertical mixing under lower boundary layer
579 conditions.

580 FIGAERO-OA explained about 13% of BBOA in AMS OA during the campaign and this ratio
581 remained relatively stable across different periods compared with daytime SOA (Fig. 8 a and b).
582 Because BBOA is closely tied to local biomass burning activities, air mass variations likely had
583 only a minor influence on its chemical characteristics. BB-LVOA showed a diurnal pattern similar
584 to both BBOA in AMS-OA and levoglucosan (Fig. 9a), with an evening peak around 18:30 LT,
585 confirming their close association with biomass burning emissions. For nighttime chemistry related
586 factor, both Night-OA (from AMS) and Night-LVOA (from thermograms) increase during the
587 nighttime, while they did not share a similar diurnal pattern (Fig. 9b). Night-LVOA peaked at about
588 20:00 LT and decreased after 4:00 LT, while Night-OA peaked later, at about 06:00 LT, and declined

589 in the morning. It suggested that Night-LVOA identified by FIGAERO-CIMS might not be able to
590 fully capture the evolution of organic compounds involved in nighttime chemistry, which can
591 explain 48% of Night-OA in AMS-OA. Given that the majority of organic compounds formed
592 through the nighttime chemistry were oxygenated and could be detected by FIGAERO CIMS (Wu
593 et al., 2021), we speculated that the volatility of organic compounds decreased overnight, resulting
594 that some low volatility organic aerosols would not be fully vaporized during the heating process.
595 Xu et al. (2019) found that nighttime MO-OOA exhibited lower volatility compared with daytime
596 MO-OOA, likely due to differences in precursors, formation mechanisms, and meteorological
597 conditions.

598 **4. Conclusion**

599 In this study, we applied a PMF analysis to field thermogram data set measured by the
600 FIGAERO-CIMS and classified the factors based on their potential formation pathways and
601 volatility. Based on the PMF analysis to thermograms data sets, six daytime OA factors, a biomass
602 burning related factor, and nighttime chemistry related factor were identified. The formation of Day-
603 HNO_x -LVOA and Day- LNO_x -LVOA was closely related to gas-particle partitioning, while Day-
604 HNO_x -LVOA was observed to be formed with organic vapors under high NO_x condition. The
605 increase in NO_x concentration might inhibit the production of highly oxygenated compounds (Cai
606 et al., 2024), which could explain the relatively high volatility of Day- HNO_x -LVOA. Two urban
607 related factors, Day-urban-LVOA and Day-urban-ELVOA, were identified, which only showed a
608 daytime enhancement in urban plumes. The former might originate from aqueous processes, while
609 the latter was likely formed through gas-particle partitioning. Our results demonstrated that
610 photochemical-derived gas-particle partitioning mainly contributed to OA formation in downwind
611 urban plumes.

612 Daytime aging processes of organic aerosol were observed and leading to the decrease in
613 volatility with two aged factors (Day-aged-LVOA and Day-aged-ELVOA) identified. The formation
614 of Day-aged-LVOA was related to the photochemical aging processes of Day- HNO_x -LVOA, Day-
615 LNO_x -LVOA, Day-urban-LVOA, and Day-urban-ELVOA, while Day-aged-ELVOA originates
616 from the aging processes of Day- LNO_x -LVOA, Day-urban-LVOA, and Day-urban-ELVOA. In
617 general, these six thermogram daytime factors could explain the majority of daytime SOA in AMS

618 OA, and this ratio increase from 79% during the long-range transport period to 85% during the
619 urban air masses period, probably owing to a higher OA volatility (Cai et al., 2024). While
620 FIGAERO-OA is unable to explain hydrocarbon like OA (HOA) and more oxygenated OA (MOOA),
621 since the FIGAERO-CIMS could not detect hydrocarbon molecules and low volatility organic
622 compounds with a volatilization temperature higher than 170 °C. For biomass-related OA, BB-
623 LVOA could explain about 11%-13% of the BBOA in AMS OA, sharing a similar diurnal pattern,
624 indicating that adopting a PMF analysis to thermogram profile could capture biomass burning events.
625 While Night-LVOA had a different diurnal pattern with Night-OA in AMS OA, implying that this
626 thermogram factor was not unable to represent the evolution of OA during the nighttime.

627 To our knowledge, existing field studies applying PMF to FIGAERO-CIMS data have
628 primarily focused on the mass concentrations or signal intensities of organic compounds rather than
629 their thermograms. Chen et al. (2020) applied PMF to FIGAERO-CIMS datasets collected in
630 Yorkville, GA, and reported substantial contributions of isoprene- and monoterpene-derived SOA
631 during both daytime and nighttime. Using the same approach, Ye et al. (2023) showed that low-NO-
632 like oxidation pathways played a significant role in SOA formation in urban environments. However,
633 these PMF analyses did not provide volatility information, which limits our ability to fully
634 understand the formation mechanisms and aging processes of OA. Lee et al. (2020) demonstrated
635 that combining molecular-level composition measurements with volatility information enables the
636 resolution of organic aerosol formation and aging pathways in the atmosphere, providing direct
637 constraints on how oxidation processes alter both chemical functionality and volatility during
638 aerosol evolution. Buchholz et al. (2020) performed PMF analysis on FIGAERO-CIMS
639 thermogram datasets in laboratory experiments and demonstrated that both OA volatility and
640 composition varied with relative humidity. Nevertheless, applications of thermogram-based PMF to
641 ambient field measurements remain scarce.

642 Our results show that applying PMF directly to thermogram profiles from field observations
643 yields additional and valuable volatility information that is not accessible from traditional mass- or
644 signal-based PMF analyses. This added dimension is particularly useful for OA source
645 apportionment. Along with PMF analysis of AMS or ACSM data, it can provide crucial information
646 in understanding the formation and aging processes of OA. Using this method, we found that the
647 daytime atmospheric evolution of SOA involved gas–particle partitioning, aqueous-phase reactions,

648 and photochemical aging, highlighting the complexity of daytime SOA formation. Moreover, SOA
649 volatility was strongly dependent on its formation pathways. variations in NO_x not only influenced
650 atmospheric oxidation but also modified SOA volatility by altering formation mechanisms.
651 Nevertheless, further investigations are required to clarify the role of urban plumes in shaping SOA
652 formation and its physicochemical properties.

653

654

655 *Data availability.* Data from the measurements are available at 10.6084/m9.figshare.30155584

656

657 *Supplement.* The supplement related to this article is available online at xxx.

658

659 *Author contributions.* M.C., W. H., and B.Y. designed the research. M.C., B.Y., W.H., Y.C., S. H.,
660 S.Y., W.C., Y. P., and J.Z. performed the measurements. M. C., B.Y., W.H., Y.C., S. H., Z. D., and
661 D. C. analyzed the data. M. C., W.H. and B.Y. wrote the paper with contributions from all co-authors.

662

663 *Competing interests.* The authors declare that they have no conflict of interest.

664

665 *Financial support.* This work was supported by Guangdong Basic and Applied Basic Research
666 Foundation (grant nos. 2024A1515030221, 2023A1515012240), National Natural Science
667 Foundation of China (grant no. 42305123, 42375105), Science and Technology Projects in
668 Guangzhou (grant no. 2025A04J4493), the Key Innovation Team of Guangdong Meteorological
669 Bureau (No. GRMCTD202506-ZD06) , and Central Public interest Scientific Institution Basal
670 Research Fund of South China Institute of Environmental Sciences, MEE (grant no. PM-zx097-
671 202506-214).

672

673 Reference

674 Al-Naiema, I. M., Hettiyadura, A. P. S., Wallace, H. W., Sanchez, N. P., Madler, C. J., Cevik, B. K.,
675 Bui, A. A. T., Kettler, J., Griffin, R. J., and Stone, E. A.: Source apportionment of fine particulate matter
676 in Houston, Texas: insights to secondary organic aerosols, *Atmos. Chem. Phys.*, 18, 15601-15622,
677 10.5194/acp-18-15601-2018, 2018.

678 Apte, J. S., Brauer, M., Cohen, A. J., Ezzati, M., and Pope, C. A., III: Ambient PM_{2.5} Reduces
679 Global and Regional Life Expectancy, *Environmental Science & Technology Letters*, 5, 546-551,
680 10.1021/acs.estlett.8b00360, 2018.

681 Arias, P. A., Bellouin, N., Coppola, E., Jones, R. G., Krinner, G., Marotzke, J., Naik, V., Palmer, M.
682 D., Plattner, G. K., Rogelj, J., Rojas, M., Sillmann, J., Storelvmo, T., Thorne, P. W., Trewin, B., Achuta
683 Rao, K., Adhikary, B., Allan, R. P., Armour, K., Bala, G., Barimalala, R., Berger, S., Canadell, J. G.,
684 Cassou, C., Cherchi, A., Collins, W., Collins, W. D., Connors, S. L., Corti, S., Cruz, F., Dentener, F. J.,
685 Dereczynski, C., Di Luca, A., Diongue Niang, A., Doblas-Reyes, F. J., Dosio, A., Douville, H.,
686 Engelbrecht, F., Eyring, V., Fischer, E., Forster, P., Fox-Kemper, B., Fuglestvedt, J. S., Fyfe, J. C., Gillett,
687 N. P., Goldfarb, L., Gorodetskaya, I., Gutierrez, J. M., Hamdi, R., Hawkins, E., Hewitt, H. T., Hope, P.,
688 Islam, A. S., Jones, C., Kaufman, D. S., Kopp, R. E., Kosaka, Y., Kossin, J., Krakovska, S., Lee, J. Y., Li,
689 J., Mauritzen, T., Maycock, T. K., Meinshausen, M., Min, S. K., Monteiro, P. M. S., Ngo-Duc, T., Otto,
690 F., Pinto, I., Pirani, A., Raghavan, K., Ranasinghe, R., Ruane, A. C., Ruiz, L., Sallée, J. B., Samset, B.
691 H., Sathyendranath, S., Seneviratne, S. I., Sörensson, A. A., Szopa, S., Takayabu, I., Tréguier, A. M., van
692 den Hurk, B., Vautard, R., von Schuckmann, K., Zaehle, S., Zhang, X., and Zickfeld, K.: Technical
693 Summary, in: *Climate Change 2021: The Physical Science Basis. Contribution of Working Group I to the Sixth Assessment Report of the Intergovernmental Panel on Climate Change*, edited by: Masson-
694 Delmotte, V., Zhai, P., Pirani, A., Connors, S. L., Péan, C., Berger, S., Caud, N., Chen, Y., Goldfarb, L.,
695 Gomis, M. I., Huang, M., Leitzell, K., Lonnoy, E., Matthews, J. B. R., Maycock, T. K., Waterfield, T.,
696 Yelekçi, O., Yu, R., and Zhou, B., Cambridge University Press, Cambridge, United Kingdom and New
697 York, NY, USA, 33–144, 10.1017/9781009157896.002, 2021.

698 Barsanti, K. C. and Pankow, J. F.: Thermodynamics of the formation of atmospheric organic
699 particulate matter by accretion reactions—Part 1: aldehydes and ketones, *Atmospheric Environment*, 38,
700 4371-4382, <https://doi.org/10.1016/j.atmosenv.2004.03.035>, 2004.

701 Buchholz, A., Ylisirniö, A., Huang, W., Mohr, C., Canagaratna, M., Worsnop, D. R., Schobesberger,
702 S., and Virtanen, A.: Deconvolution of FIGAERO–CIMS thermal desorption profiles using positive
703 matrix factorisation to identify chemical and physical processes during particle evaporation, *Atmos.
704 Chem. Phys.*, 20, 7693-7716, 10.5194/acp-20-7693-2020, 2020.

705 Cai, M., Ye, C., Yuan, B., Huang, S., Zheng, E., Yang, S., Wang, Z., Lin, Y., Li, T., Hu, W., Chen,
706 W., Song, Q., Li, W., Peng, Y., Liang, B., Sun, Q., Zhao, J., Chen, D., Sun, J., Yang, Z., and Shao, M.:
707 Enhanced daytime secondary aerosol formation driven by gas–particle partitioning in downwind urban
708 plumes, *Atmos. Chem. Phys.*, 24, 13065-13079, 10.5194/acp-24-13065-2024, 2024.

709 Cai, Y., Ye, C., Chen, W., Hu, W., Song, W., Peng, Y., Huang, S., Qi, J., Wang, S., Wang, C., Wu, C.,
710 Wang, Z., Wang, B., Huang, X., He, L., Gligorovski, S., Yuan, B., Shao, M., and Wang, X.: The important
711 contribution of secondary formation and biomass burning to oxidized organic nitrogen (OON) in a
712 polluted urban area: insights from in situ measurements of a chemical ionization mass spectrometer
713 (CIMS), *Atmos. Chem. Phys.*, 23, 8855-8877, 10.5194/acp-23-8855-2023, 2023.

714 Chacon-Madrid, H. J. and Donahue, N. M.: Fragmentation vs. functionalization: chemical aging

715

716 and organic aerosol formation, *Atmos. Chem. Phys.*, 11, 10553-10563, 10.5194/acp-11-10553-2011,
717 2011.

718 Charan, S. M., Huang, Y., and Seinfeld, J. H.: Computational Simulation of Secondary Organic
719 Aerosol Formation in Laboratory Chambers, *Chemical Reviews*, 119, 11912-11944,
720 10.1021/acs.chemrev.9b00358, 2019.

721 Canonaco, F., Crippa, M., Slowik, J. G., Baltensperger, U., and Prévôt, A. S. H.: SoFi, an IGOR-
722 based interface for the efficient use of the generalized multilinear engine (ME-2) for the source
723 apportionment: ME-2 application to aerosol mass spectrometer data, *Atmos. Meas. Tech.*, 6, 3649-3661,
724 10.5194/amt-6-3649-2013, 2013.

725 Chen, G., Sosedova, Y., Canonaco, F., Fröhlich, R., Tobler, A., Vlachou, A., Daellenbach, K. R.,
726 Bozzetti, C., Hueglin, C., Graf, P., Baltensperger, U., Slowik, J. G., El Haddad, I., and Prévôt, A. S. H.:
727 Time-dependent source apportionment of submicron organic aerosol for a rural site in an alpine valley
728 using a rolling positive matrix factorisation (PMF) window, *Atmos. Chem. Phys.*, 21, 15081-15101,
729 10.5194/acp-21-15081-2021, 2021a.

730 Chen, W. T., Shao, M., Lu, S. H., Wang, M., Zeng, L. M., Yuan, B., and Liu, Y.: Understanding
731 primary and secondary sources of ambient carbonyl compounds in Beijing using the PMF model, *Atmos.*
732 *Chem. Phys.*, 14, 3047-3062, 10.5194/acp-14-3047-2014, 2014.

733 Chen, W., Hu, W., Tao, Z., Cai, Y., Cai, M., Zhu, M., Ye, Y., Zhou, H., Jiang, H., Li, J., Song, W.,
734 Zhou, J., Huang, S., Yuan, B., Shao, M., Feng, Q., Li, Y., Isaacman-VanWertz, G., Stark, H., Day, D. A.,
735 Campuzano-Jost, P., Jimenez, J. L., and Wang, X.: Quantitative Characterization of the Volatility
736 Distribution of Organic Aerosols in a Polluted Urban Area: Intercomparison Between Thermodenuder
737 and Molecular Measurements, *Journal of Geophysical Research: Atmospheres*, 129, e2023JD040284,
738 <https://doi.org/10.1029/2023JD040284>, 2024.

739 Chen, Y., Guo, H., Nah, T., Tanner, D. J., Sullivan, A. P., Takeuchi, M., Gao, Z., Vasilakos, P., Russell,
740 A. G., Baumann, K., Huey, L. G., Weber, R. J., and Ng, N. L.: Low-Molecular-Weight Carboxylic Acids
741 in the Southeastern U.S.: Formation, Partitioning, and Implications for Organic Aerosol Aging,
742 *Environmental Science & Technology*, 55, 6688-6699, 10.1021/acs.est.1c01413, 2021b.

743 Chen, Y., Takeuchi, M., Nah, T., Xu, L., Canagaratna, M. R., Stark, H., Baumann, K., Canonaco, F.,
744 Prévôt, A. S. H., Huey, L. G., Weber, R. J., and Ng, N. L.: Chemical characterization of secondary organic
745 aerosol at a rural site in the southeastern US: insights from simultaneous high-resolution time-of-flight
746 aerosol mass spectrometer (HR-ToF-AMS) and FIGAERO chemical ionization mass spectrometer
747 (CIMS) measurements, *Atmos. Chem. Phys.*, 20, 8421-8440, 10.5194/acp-20-8421-2020, 2020.

748 Decker, Z. C. J., Zarzana, K. J., Coggon, M., Min, K.-E., Pollack, I., Ryerson, T. B., Peischl, J.,
749 Edwards, P., Dubé, W. P., Markovic, M. Z., Roberts, J. M., Veres, P. R., Graus, M., Warneke, C., de Gouw,
750 J., Hatch, L. E., Barsanti, K. C., and Brown, S. S.: Nighttime Chemical Transformation in Biomass
751 Burning Plumes: A Box Model Analysis Initialized with Aircraft Observations, *Environmental Science
& Technology*, 53, 2529-2538, 10.1021/acs.est.8b05359, 2019.

753 Donahue, N. M., Epstein, S. A., Pandis, S. N., and Robinson, A. L.: A two-dimensional volatility
754 basis set: 1. organic-aerosol mixing thermodynamics, *Atmos. Chem. Phys.*, 11, 3303-3318, 10.5194/acp-
755 11-3303-2011, 2011.

756 Donahue, N. M., Kroll, J. H., Pandis, S. N., and Robinson, A. L.: A two-dimensional volatility basis
757 set – Part 2: Diagnostics of organic-aerosol evolution, *Atmos. Chem. Phys.*, 12, 615-634, 10.5194/acp-
758 12-615-2012, 2012.

759 Faxon, C., Hammes, J., Le Breton, M., Pathak, R. K., and Hallquist, M.: Characterization of organic

760 nitrate constituents of secondary organic aerosol (SOA) from nitrate-radical-initiated oxidation of
761 limonene using high-resolution chemical ionization mass spectrometry, *Atmos. Chem. Phys.*, 18, 5467-
762 5481, 10.5194/acp-18-5467-2018, 2018.

763 Feng, T., Wang, Y., Hu, W., Zhu, M., Song, W., Chen, W., Sang, Y., Fang, Z., Deng, W., Fang, H.,
764 Yu, X., Wu, C., Yuan, B., Huang, S., Shao, M., Huang, X., He, L., Lee, Y. R., Huey, L. G., Canonaco, F.,
765 Prevot, A. S. H., and Wang, X.: Impact of aging on the sources, volatility, and viscosity of organic
766 aerosols in Chinese outflows, *Atmos. Chem. Phys.*, 23, 611-636, 10.5194/acp-23-611-2023, 2023.

767 Fisher, J. A., Jacob, D. J., Travis, K. R., Kim, P. S., Marais, E. A., Chan Miller, C., Yu, K., Zhu, L.,
768 Yantosca, R. M., Sulprizio, M. P., Mao, J., Wennberg, P. O., Crounse, J. D., Teng, A. P., Nguyen, T. B.,
769 St. Clair, J. M., Cohen, R. C., Romer, P., Nault, B. A., Wooldridge, P. J., Jimenez, J. L., Campuzano-Jost,
770 P., Day, D. A., Hu, W., Shepson, P. B., Xiong, F., Blake, D. R., Goldstein, A. H., Misztal, P. K., Hanisco,
771 T. F., Wolfe, G. M., Ryerson, T. B., Wisthaler, A., and Mikoviny, T.: Organic nitrate chemistry and its
772 implications for nitrogen budgets in an isoprene- and monoterpene-rich atmosphere: constraints from
773 aircraft (SEAC4RS) and ground-based (SOAS) observations in the Southeast US, *Atmos. Chem. Phys.*,
774 16, 5969-5991, 10.5194/acp-16-5969-2016, 2016.

775 Gaston, C. J., Lopez-Hilfiker, F. D., Whybrey, L. E., Hadley, O., McNair, F., Gao, H., Jaffe, D. A.,
776 and Thornton, J. A.: Online molecular characterization of fine particulate matter in Port Angeles, WA:
777 Evidence for a major impact from residential wood smoke, *Atmospheric Environment*, 138, 99-107,
778 <https://doi.org/10.1016/j.atmosenv.2016.05.013>, 2016.

779 Graham, E. L., Wu, C., Bell, D. M., Bertrand, A., Haslett, S. L., Baltensperger, U., El Haddad, I.,
780 Krejci, R., Riipinen, I., and Mohr, C.: Volatility of aerosol particles from NO₃ oxidation of various
781 biogenic organic precursors, *Atmos. Chem. Phys.*, 23, 7347-7362, 10.5194/acp-23-7347-2023, 2023.

782 Guo, J., Zhou, S., Cai, M., Zhao, J., Song, W., Zhao, W., Hu, W., Sun, Y., He, Y., Yang, C., Xu, X.,
783 Zhang, Z., Cheng, P., Fan, Q., Hang, J., Fan, S., Wang, X., and Wang, X.: Characterization of submicron
784 particles by time-of-flight aerosol chemical speciation monitor (ToF-ACSM) during wintertime: aerosol
785 composition, sources, and chemical processes in Guangzhou, China, *Atmos. Chem. Phys.*, 20, 7595-7615,
786 10.5194/acp-20-7595-2020, 2020.

787 Hildebrandt Ruiz, L., Paciga, A. L., Cerully, K. M., Nenes, A., Donahue, N. M., and Pandis, S. N.:
788 Formation and aging of secondary organic aerosol from toluene: changes in chemical composition,
789 volatility, and hygroscopicity, *Atmos. Chem. Phys.*, 15, 8301-8313, 10.5194/acp-15-8301-2015, 2015.

790 Huang, R.-J., Zhang, Y., Bozzetti, C., Ho, K.-F., Cao, J.-J., Han, Y., Daellenbach, K. R., Slowik, J.
791 G., Platt, S. M., Canonaco, F., Zotter, P., Wolf, R., Pieber, S. M., Bruns, E. A., Crippa, M., Ciarelli, G.,
792 Piazzalunga, A., Schwikowski, M., Abbaszade, G., Schnelle-Kreis, J., Zimmermann, R., An, Z., Szidat,
793 S., Baltensperger, U., Haddad, I. E., and Prevot, A. S. H.: High secondary aerosol contribution to
794 particulate pollution during haze events in China, *Nature*, 514, 218-222, 10.1038/nature13774
795 <http://www.nature.com/nature/journal/vaop/ncurrent/abs/nature13774.html#supplementary-information>, 2014.

797 Huang, S., Wu, Z., Poulain, L., van Pinxteren, M., Merkel, M., Assmann, D., Herrmann, H., and
798 Wiedensohler, A.: Source apportionment of the organic aerosol over the Atlantic Ocean from
799 53°N to 53°S: significant contributions from marine emissions and long-range transport,
800 *Atmos. Chem. Phys.*, 18, 18043-18062, 10.5194/acp-18-18043-2018, 2018.

801 Huang, W., Saathoff, H., Shen, X., Ramisetty, R., Leisner, T., and Mohr, C.: Seasonal characteristics
802 of organic aerosol chemical composition and volatility in Stuttgart, Germany, *Atmos. Chem. Phys.*, 19,
803 11687-11700, 10.5194/acp-19-11687-2019, 2019.

804 Huang, X. F., He, L. Y., Hu, M., Canagaratna, M. R., Sun, Y., Zhang, Q., Zhu, T., Xue, L., Zeng, L.
805 W., Liu, X. G., Zhang, Y. H., Jayne, J. T., Ng, N. L., and Worsnop, D. R.: Highly time-resolved chemical
806 characterization of atmospheric submicron particles during 2008 Beijing Olympic Games using an
807 Aerodyne High-Resolution Aerosol Mass Spectrometer, *Atmos. Chem. Phys.*, 10, 8933-8945,
808 10.5194/acp-10-8933-2010, 2010.

809 Iyer, S., Lopez-Hilfiker, F., Lee, B. H., Thornton, J. A., and Kurtén, T.: Modeling the Detection of
810 Organic and Inorganic Compounds Using Iodide-Based Chemical Ionization, *The Journal of Physical
811 Chemistry A*, 120, 576-587, 10.1021/acs.jpca.5b09837, 2016.

812 Jenkin, M. E.: Modelling the formation and composition of secondary organic aerosol from α - and
813 β -pinene ozonolysis using MCM v3, *Atmos. Chem. Phys.*, 4, 1741-1757, 10.5194/acp-4-1741-2004,
814 2004.

815 Jimenez, J. L., Canagaratna, M., Donahue, N., Prevot, A., Zhang, Q., Kroll, J. H., DeCarlo, P. F.,
816 Allan, J. D., Coe, H., and Ng, N. J. S.: Evolution of organic aerosols in the atmosphere, 326, 1525-1529,
817 2009.

818 Jorga, S. D., Florou, K., Kaltsonoudis, C., Kodros, J. K., Vasilakopoulou, C., Cirtog, M., Fouqueau,
819 A., Picquet-Varrault, B., Nenes, A., and Pandis, S. N.: Nighttime chemistry of biomass burning emissions
820 in urban areas: A dual mobile chamber study, *Atmos. Chem. Phys.*, 21, 15337-15349, 10.5194/acp-21-
821 15337-2021, 2021.

822 Kiendler-Scharr, A., Mensah, A. A., Fries, E., Topping, D., Nemitz, E., Prevot, A. S. H., Äijälä, M.,
823 Allan, J., Canonaco, F., Canagaratna, M., Carbone, S., Crippa, M., Dall Osto, M., Day, D. A., De Carlo,
824 P., Di Marco, C. F., Elbern, H., Eriksson, A., Freney, E., Hao, L., Herrmann, H., Hildebrandt, L., Hillamo,
825 R., Jimenez, J. L., Laaksonen, A., McFiggans, G., Mohr, C., O'Dowd, C., Otjes, R., Ovadnevaite, J.,
826 Pandis, S. N., Poulain, L., Schlag, P., Sellegrí, K., Swietlicki, E., Tiitta, P., Vermeulen, A., Wahner, A.,
827 Worsnop, D., and Wu, H. C.: Ubiquity of organic nitrates from nighttime chemistry in the European
828 submicron aerosol, *Geophysical Research Letters*, 43, 7735-7744,
829 <https://doi.org/10.1002/2016GL069239>, 2016.

830 Krieger, U. K., Siegrist, F., Marcolli, C., Emanuelsson, E. U., Gøbel, F. M., Bilde, M., Marsh, A.,
831 Reid, J. P., Huisman, A. J., Riipinen, I., Hyttinen, N., Myllys, N., Kurtén, T., Bannan, T., Percival, C. J.,
832 and Topping, D.: A reference data set for validating vapor pressure measurement techniques: homologous
833 series of polyethylene glycols, *Atmos. Meas. Tech.*, 11, 49-63, 10.5194/amt-11-49-2018, 2018.

834 Kroll, J. H. and Seinfeld, J. H.: Chemistry of secondary organic aerosol: Formation and evolution
835 of low-volatility organics in the atmosphere, *Atmospheric Environment*, 42, 3593-3624,
836 <https://doi.org/10.1016/j.atmosenv.2008.01.003>, 2008.

837 Kuang, Y., Huang, S., Xue, B., Luo, B., Song, Q., Chen, W., Hu, W., Li, W., Zhao, P., Cai, M., Peng,
838 Y., Qi, J., Li, T., Wang, S., Chen, D., Yue, D., Yuan, B., and Shao, M.: Contrasting effects of secondary
839 organic aerosol formations on organic aerosol hygroscopicity, *Atmos. Chem. Phys.*, 21, 10375-10391,
840 10.5194/acp-21-10375-2021, 2021.

841 Lee, B. H., D'Ambro, E. L., Lopez-Hilfiker, F. D., Schobesberger, S., Mohr, C., Zawadowicz, M.
842 A., Liu, J., Shilling, J. E., Hu, W., Palm, B. B., Jimenez, J. L., Hao, L., Virtanen, A., Zhang, H., Goldstein,
843 A. H., Pye, H. O. T., and Thornton, J. A.: Resolving Ambient Organic Aerosol Formation and Aging
844 Pathways with Simultaneous Molecular Composition and Volatility Observations, *ACS Earth and Space
845 Chemistry*, 4, 391-402, 10.1021/acsearthspacechem.9b00302, 2020.

846 Lee, B. H., Lopez-Hilfiker, F. D., Mohr, C., Kurtén, T., Worsnop, D. R., and Thornton, J. A.: An
847 Iodide-Adduct High-Resolution Time-of-Flight Chemical-Ionization Mass Spectrometer: Application to

848 Atmospheric Inorganic and Organic Compounds, Environmental Science & Technology, 48, 6309-6317,
849 10.1021/es500362a, 2014.

850 Lee, B. P., Li, Y. J., Yu, J. Z., Louie, P. K., and Chan, C. K.: Characteristics of submicron particulate
851 matter at the urban roadside in downtown Hong Kong—Overview of 4 months of continuous high-
852 resolution aerosol mass spectrometer measurements, Journal of Geophysical Research: Atmospheres,
853 120, 7040-7058, 2015.

854 Lopez-Hilfiker, F. D., Iyer, S., Mohr, C., Lee, B. H., D'Ambro, E. L., Kurtén, T., and Thornton, J.
855 A.: Constraining the sensitivity of iodide adduct chemical ionization mass spectrometry to
856 multifunctional organic molecules using the collision limit and thermodynamic stability of iodide ion
857 adducts, Atmos. Meas. Tech., 9, 1505-1512, 10.5194/amt-9-1505-2016, 2016.

858 Lopez-Hilfiker, F. D., Mohr, C., Ehn, M., Rubach, F., Kleist, E., Wildt, J., Mentel, T. F., Lutz, A.,
859 Hallquist, M., Worsnop, D., and Thornton, J. A.: A novel method for online analysis of gas and particle
860 composition: description and evaluation of a Filter Inlet for Gases and AEROsols (FIGAERO), Atmos.
861 Meas. Tech., 7, 983-1001, 10.5194/amt-7-983-2014, 2014.

862 Louvaris, E. E., Florou, K., Karnezi, E., Papanastasiou, D. K., Gkatzelis, G. I., and Pandis, S. N.:
863 Volatility of source apportioned wintertime organic aerosol in the city of Athens, Atmospheric
864 Environment, 158, 138-147, <https://doi.org/10.1016/j.atmosenv.2017.03.042>, 2017.

865 Lu, Q., Murphy, B. N., Qin, M., Adams, P. J., Zhao, Y., Pye, H. O. T., Efstathiou, C., Allen, C., and
866 Robinson, A. L.: Simulation of organic aerosol formation during the CalNex study: updated mobile
867 emissions and secondary organic aerosol parameterization for intermediate-volatility organic compounds,
868 Atmos. Chem. Phys., 20, 4313-4332, 10.5194/acp-20-4313-2020, 2020.

869 Matsui, H., Koike, M., Takegawa, N., Kondo, Y., Griffin, R. J., Miyazaki, Y., Yokouchi, Y., and
870 Ohara, T.: Secondary organic aerosol formation in urban air: Temporal variations and possible
871 contributions from unidentified hydrocarbons, Journal of Geophysical Research: Atmospheres, 114,
872 <https://doi.org/10.1029/2008JD010164>, 2009.

873 Nie, W., Yan, C., Huang, D. D., Wang, Z., Liu, Y., Qiao, X., Guo, Y., Tian, L., Zheng, P., Xu, Z., Li,
874 Y., Xu, Z., Qi, X., Sun, P., Wang, J., Zheng, F., Li, X., Yin, R., Dallenbach, K. R., Bianchi, F., Petäjä, T.,
875 Zhang, Y., Wang, M., Schervish, M., Wang, S., Qiao, L., Wang, Q., Zhou, M., Wang, H., Yu, C., Yao, D.,
876 Guo, H., Ye, P., Lee, S., Li, Y. J., Liu, Y., Chi, X., Kerminen, V.-M., Ehn, M., Donahue, N. M., Wang, T.,
877 Huang, C., Kulmala, M., Worsnop, D., Jiang, J., and Ding, A.: Secondary organic aerosol formed by
878 condensing anthropogenic vapours over China's megacities, Nature Geoscience, 15, 255-261,
879 10.1038/s41561-022-00922-5, 2022.

880 Nie, W., Yan, C., Yang, L., Roldin, P., Liu, Y., Vogel, A. L., Molteni, U., Stolzenburg, D.,
881 Finkenzeller, H., Amorim, A., Bianchi, F., Curtius, J., Dada, L., Draper, D. C., Duplissy, J., Hansel, A.,
882 He, X.-C., Hofbauer, V., Jokinen, T., Kim, C., Lehtipalo, K., Nichman, L., Mauldin, R. L., Makhmutov,
883 V., Mentler, B., Mizelli-Ojedanic, A., Petäjä, T., Quéléver, L. L. J., Schallhart, S., Simon, M., Tauber, C.,
884 Tomé, A., Volkamer, R., Wagner, A. C., Wagner, R., Wang, M., Ye, P., Li, H., Huang, W., Qi, X., Lou, S.,
885 Liu, T., Chi, X., Dommen, J., Baltensperger, U., El Haddad, I., Kirkby, J., Worsnop, D., Kulmala, M.,
886 Donahue, N. M., Ehn, M., and Ding, A.: NO at low concentration can enhance the formation of highly
887 oxygenated biogenic molecules in the atmosphere, Nature Communications, 14, 3347, 10.1038/s41467-
888 023-39066-4, 2023.

889 Nihill, K. J., Ye, Q., Majluf, F., Krechmer, J. E., Canagaratna, M. R., and Kroll, J. H.: Influence of
890 the NO/NO₂ Ratio on Oxidation Product Distributions under High-NO Conditions, Environmental
891 Science & Technology, 55, 6594-6601, 10.1021/acs.est.0c07621, 2021.

Ou, H. J., Cai, M. F., Liang, B. L., Sun, Q. B., Zhou, S. Z., Xu, Y. S., Ren, L. H., and Zhao, J.: Characterization, Sources, and Chemical Processes of Submicron Aerosols at a Mountain Site in Central China, *Journal of Geophysical Research: Atmospheres*, 128, e2022JD038258, <https://doi.org/10.1029/2022JD038258>, 2023.

Paatero, P. and Tapper, U.: Positive matrix factorization: A non-negative factor model with optimal utilization of error estimates of data values, *Environmetrics*, 5, 111-126, <https://doi.org/10.1002/env.3170050203>, 1994.

Pankow, J. F. and Asher, W. E.: SIMPOL.1: a simple group contribution method for predicting vapor pressures and enthalpies of vaporization of multifunctional organic compounds, *Atmos. Chem. Phys.*, 8, 2773-2796, 10.5194/acp-8-2773-2008, 2008.

Paulot, F., Crounse, J. D., Kjaergaard, H. G., Kroll, J. H., Seinfeld, J. H., and Wennberg, P. O.: Isoprene photooxidation: new insights into the production of acids and organic nitrates, *Atmos. Chem. Phys.*, 9, 1479-1501, 10.5194/acp-9-1479-2009, 2009.

Praske, E., Otkjær, R. V., Crounse, J. D., Hethcox, J. C., Stoltz, B. M., Kjaergaard, H. G., and Wennberg, P. O.: Atmospheric autoxidation is increasingly important in urban and suburban North America, *Proceedings of the National Academy of Sciences*, 115, 64-69, 10.1073/pnas.1715540115, 2018.

Pye, H. O. T., D'Ambro, E. L., Lee, B. H., Schobesberger, S., Takeuchi, M., Zhao, Y., Lopez-Hilfiker, F., Liu, J., Shilling, J. E., Xing, J., Mathur, R., Middlebrook, A. M., Liao, J., Welti, A., Graus, M., Warneke, C., de Gouw, J. A., Holloway, J. S., Ryerson, T. B., Pollack, I. B., and Thornton, J. A.: Anthropogenic enhancements to production of highly oxygenated molecules from autoxidation, *Proceedings of the National Academy of Sciences*, 116, 6641-6646, 10.1073/pnas.1810774116, 2019.

Qin, Y. M., Tan, H. B., Li, Y. J., Schurman, M. I., Li, F., Canonaco, F., Prévôt, A. S. H., and Chan, C. K.: The role of traffic emissions in particulate organics and nitrate at a downwind site in the periphery of Guangzhou, China, *Atmospheric Chemistry & Physics*, 1-31, 2017.

Ren, S., Yao, L., Wang, Y., Yang, G., Liu, Y., Li, Y., Lu, Y., Wang, L., and Wang, L.: Volatility parameterization of ambient organic aerosols at a rural site of the North China Plain, *Atmos. Chem. Phys.*, 22, 9283-9297, 10.5194/acp-22-9283-2022, 2022.

Rissanen, M. P.: NO₂ Suppression of Autoxidation–Inhibition of Gas-Phase Highly Oxidized Dimer Product Formation, *ACS Earth and Space Chemistry*, 2, 1211-1219, 10.1021/acsearthspacechem.8b00123, 2018.

Rudich, Y., Donahue, N. M., and Mentel, T. F.: Aging of Organic Aerosol: Bridging the Gap Between Laboratory and Field Studies, *Annual Review of Physical Chemistry*, 58, 321-352, <https://doi.org/10.1146/annurev.physchem.58.032806.104432>, 2007.

Shrivastava, M., Andreae, M. O., Artaxo, P., Barbosa, H. M. J., Berg, L. K., Brito, J., Ching, J., Easter, R. C., Fan, J., Fast, J. D., Feng, Z., Fuentes, J. D., Glasius, M., Goldstein, A. H., Alves, E. G., Gomes, H., Gu, D., Guenther, A., Jathar, S. H., Kim, S., Liu, Y., Lou, S., Martin, S. T., McNeill, V. F., Medeiros, A., de Sá, S. S., Shilling, J. E., Springston, S. R., Souza, R. A. F., Thornton, J. A., Isaacman-VanWertz, G., Yee, L. D., Ynoue, R., Zaveri, R. A., Zelenyuk, A., and Zhao, C.: Urban pollution greatly enhances formation of natural aerosols over the Amazon rainforest, *Nature Communications*, 10, 1046, 10.1038/s41467-019-08909-4, 2019.

Thornton, J. A., Mohr, C., Schobesberger, S., D'Ambro, E. L., Lee, B. H., and Lopez-Hilfiker, F. D.: Evaluating Organic Aerosol Sources and Evolution with a Combined Molecular Composition and Volatility Framework Using the Filter Inlet for Gases and Aerosols (FIGAERO), *Accounts of Chemical*

936 Research, 53, 1415-1426, 10.1021/acs.accounts.0c00259, 2020.

937 Tian, S. L., Pan, Y. P., and Wang, Y. S.: Size-resolved source apportionment of particulate matter in
938 urban Beijing during haze and non-haze episodes, *Atmos. Chem. Phys.*, 16, 1-19, 10.5194/acp-16-1-2016,
939 2016.

940 Ulbrich, I. M., Canagaratna, M. R., Zhang, Q., Worsnop, D. R., and Jimenez, J. L.: Interpretation of
941 organic components from Positive Matrix Factorization of aerosol mass spectrometric data, *Atmos.*
942 *Chem. Phys.*, 9, 2891-2918, 10.5194/acp-9-2891-2009, 2009.

943 Walser, M. L., Park, J., Gomez, A. L., Russell, A. R., and Nizkorodov, S. A.: Photochemical Aging
944 of Secondary Organic Aerosol Particles Generated from the Oxidation of d-Limonene, *The Journal of*
945 *Physical Chemistry A*, 111, 1907-1913, 10.1021/jp0662931, 2007.

946 Wang, Y., Clusius, P., Yan, C., Dällenbach, K., Yin, R., Wang, M., He, X.-C., Chu, B., Lu, Y., Dada,
947 L., Kangasluoma, J., Rantala, P., Deng, C., Lin, Z., Wang, W., Yao, L., Fan, X., Du, W., Cai, J., Heikkinen,
948 L., Tham, Y. J., Zha, Q., Ling, Z., Junninen, H., Petäjä, T., Ge, M., Wang, Y., He, H., Worsnop, D. R.,
949 Kerminen, V.-M., Bianchi, F., Wang, L., Jiang, J., Liu, Y., Boy, M., Ehn, M., Donahue, N. M., and
950 Kulmala, M.: Molecular Composition of Oxygenated Organic Molecules and Their Contributions to
951 Organic Aerosol in Beijing, *Environmental Science & Technology*, 56, 770-778,
952 10.1021/acs.est.1c05191, 2022.

953 Ulbrich, I. M., Canagaratna, M. R., Zhang, Q., Worsnop, D. R., and Jimenez, J. L.: Interpretation of
954 organic components from Positive Matrix Factorization of aerosol mass spectrometric data, *Atmos.*
955 *Chem. Phys.*, 9, 2891-2918, 10.5194/acp-9-2891-2009, 2009.

956 Uchida, K., Ide, Y., and Takegawa, N.: Ionization efficiency of evolved gas molecules from aerosol
957 particles in a thermal desorption aerosol mass spectrometer: Laboratory experiments, *Aerosol Sci Tech*,
958 53, 86-93, 10.1080/02786826.2018.1544704, 2019.

959 Wu, C., Bell, D. M., Graham, E. L., Haslett, S., Riipinen, I., Baltensperger, U., Bertrand, A.,
960 Giannoukos, S., Schoonbaert, J., El Haddad, I., Prevot, A. S. H., Huang, W., and Mohr, C.: Photolytically
961 induced changes in composition and volatility of biogenic secondary organic aerosol from nitrate radical
962 oxidation during night-to-day transition, *Atmos. Chem. Phys.*, 21, 14907-14925, 10.5194/acp-21-14907-
963 2021, 2021.

964 Xu, L., Kollman, M. S., Song, C., Shilling, J. E., and Ng, N. L.: Effects of NO_x on the Volatility of
965 Secondary Organic Aerosol from Isoprene Photooxidation, *Environmental Science & Technology*, 48,
966 2253-2262, 10.1021/es404842g, 2014.

967 Xu, W., Chen, C., Qiu, Y., Li, Y., Zhang, Z., Karnezi, E., Pandis, S. N., Xie, C., Li, Z., Sun, J., Ma,
968 N., Xu, W., Fu, P., Wang, Z., Zhu, J., Worsnop, D. R., Ng, N. L., and Sun, Y.: Organic aerosol volatility
969 and viscosity in the North China Plain: contrast between summer and winter, *Atmos. Chem. Phys.*, 21,
970 5463-5476, 10.5194/acp-21-5463-2021, 2021.

971 Xu, X., Wang, G., Gao, Y., Zhang, S., Chen, L., Li, R., Li, Z., and Li, R.: Smog chamber study on
972 the NO_x dependence of SOA from isoprene photo-oxidation: implication on RO₂ chemistry, *Journal of*
973 *Environmental Sciences*, <https://doi.org/10.1016/j.jes.2025.05.024>, 2025.

974 Xu, W., Xie, C., Karnezi, E., Zhang, Q., Wang, J., Pandis, S. N., Ge, X., Zhang, J., An, J., Wang, Q.,
975 Zhao, J., Du, W., Qiu, Y., Zhou, W., He, Y., Li, Y., Li, J., Fu, P., Wang, Z., Worsnop, D. R., and Sun, Y.:
976 Summertime aerosol volatility measurements in Beijing, China, *Atmos. Chem. Phys.*, 19, 10205-10216,
977 10.5194/acp-19-10205-2019, 2019.

978 Xu, W., Chen, C., Qiu, Y., Li, Y., Zhang, Z., Karnezi, E., Pandis, S. N., Xie, C., Li, Z., Sun, J., Ma,
979 N., Xu, W., Fu, P., Wang, Z., Zhu, J., Worsnop, D. R., Ng, N. L., and Sun, Y.: Organic aerosol volatility

980 and viscosity in the North China Plain: contrast between summer and winter, *Atmos. Chem. Phys.*, 21,
981 5463-5476, 10.5194/acp-21-5463-2021, 2021.

982 Yang, S., Yuan, B., Peng, Y., Huang, S., Chen, W., Hu, W., Pei, C., Zhou, J., Parrish, D. D., Wang,
983 W., He, X., Cheng, C., Li, X. B., Yang, X., Song, Y., Wang, H., Qi, J., Wang, B., Wang, C., Wang, C.,
984 Wang, Z., Li, T., Zheng, E., Wang, S., Wu, C., Cai, M., Ye, C., Song, W., Cheng, P., Chen, D., Wang, X.,
985 Zhang, Z., Wang, X., Zheng, J., and Shao, M.: The formation and mitigation of nitrate pollution:
986 comparison between urban and suburban environments, *Atmos. Chem. Phys.*, 22, 4539-4556,
987 10.5194/acp-22-4539-2022, 2022.

988 Ye, C., Liu, Y., Yuan, B., Wang, Z., Lin, Y., Hu, W., Chen, W., Li, T., Song, W., Wang, X., Lv, D.,
989 Gu, D., and Shao, M.: Low-NO-like Oxidation Pathway Makes a Significant Contribution to Secondary
990 Organic Aerosol in Polluted Urban Air, *Environmental Science & Technology*, 10.1021/acs.est.3c01055,
991 2023.

992 Ye, C., Yuan, B., Lin, Y., Wang, Z., Hu, W., Li, T., Chen, W., Wu, C., Wang, C., Huang, S., Qi, J.,
993 Wang, B., Wang, C., Song, W., Wang, X., Zheng, E., Krechmer, J. E., Ye, P., Zhang, Z., Wang, X.,
994 Worsnop, D. R., and Shao, M.: Chemical characterization of oxygenated organic compounds in the gas
995 phase and particle phase using iodide CIMS with FIGAERO in urban air, *Atmos. Chem. Phys.*, 21, 8455-
996 8478, 10.5194/acp-21-8455-2021, 2021.

997 Ylisirniö, A., Barreira, L. M. F., Pullinen, I., Buchholz, A., Jayne, J., Krechmer, J. E., Worsnop, D.
998 R., Virtanen, A., and Schobesberger, S.: On the calibration of FIGAERO-ToF-CIMS: importance and
999 impact of calibrant delivery for the particle-phase calibration, *Atmos. Meas. Tech.*, 14, 355-367,
1000 10.5194/amt-14-355-2021, 2021.

1001 Ylisirniö, A., Hyttinen, N., Li, Z., Alton, M., Nissinen, A., Pullinen, I., Miettinen, P., Yli-Juuti, T.,
1002 and Schobesberger, S.: The saturation vapor pressures of higher-order polyethylene glycols and
1003 achieving a wide calibration range for volatility measurements by FIGAERO-CIMS, *Atmos. Meas. Tech.*,
1004 18, 6449-6464, 10.5194/amt-18-6449-2025, 2025.

1005 Zhang, Q., Jimenez, J. L., Canagaratna, M. R., Ulbrich, I. M., Ng, N. L., Worsnop, D. R., and Sun,
1006 Y.: Understanding atmospheric organic aerosols via factor analysis of aerosol mass spectrometry: a
1007 review, *Analytical and Bioanalytical Chemistry*, 401, 3045-3067, 10.1007/s00216-011-5355-y, 2011.

1008 Zhang, Y. L., El-Haddad, I., Huang, R. J., Ho, K. F., Cao, J. J., Han, Y., Zotter, P., Bozzetti, C.,
1009 Daellenbach, K. R., Slowik, J. G., Salazar, G., Prévôt, A. S. H., and Szidat, S.: Large contribution of
1010 fossil fuel derived secondary organic carbon to water soluble organic aerosols in winter haze in China,
1011 *Atmos. Chem. Phys.*, 18, 4005-4017, 10.5194/acp-18-4005-2018, 2018.

1012 Zhao, W., Kawamura, K., Yue, S., Wei, L., Ren, H., Yan, Y., Kang, M., Li, L., Ren, L., Lai, S., Li,
1013 J., Sun, Y., Wang, Z., and Fu, P.: Molecular distribution and compound-specific stable carbon isotopic
1014 composition of dicarboxylic acids, oxocarboxylic acids and α -dicarbonyls in PM2.5 from Beijing, China,
1015 *Atmos. Chem. Phys.*, 18, 2749-2767, 10.5194/acp-18-2749-2018, 2018.

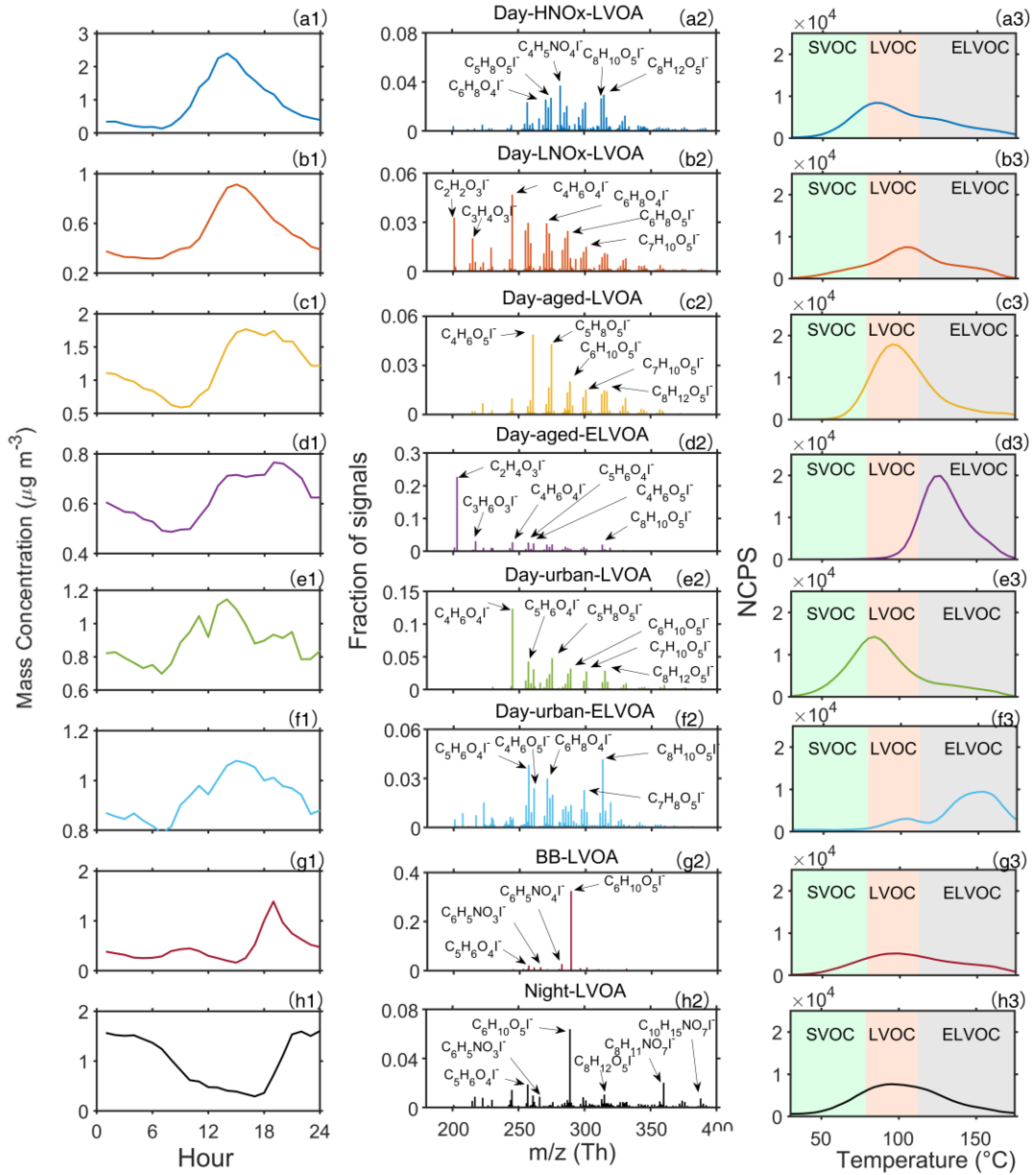
1016 Zheng, Y., Chen, Q., Cheng, X., Mohr, C., Cai, J., Huang, W., Shrivastava, M., Ye, P., Fu, P., Shi,
1017 X., Ge, Y., Liao, K., Miao, R., Qiu, X., Koenig, T. K., and Chen, S.: Precursors and Pathways Leading to
1018 Enhanced Secondary Organic Aerosol Formation during Severe Haze Episodes, *Environmental Science
& Technology*, 10.1021/acs.est.1c04255, 2021.

1019 Zhou, W., Xu, W., Kim, H., Zhang, Q., Fu, P., Worsnop, D. R., and Sun, Y.: A review of aerosol
1020 chemistry in Asia: insights from aerosol mass spectrometer measurements, *Environmental Science:
Processes & Impacts*, 22, 1616-1653, 10.1039/D0EM00212G, 2020.

1023 **Table 1.** The average volatility ($\log_{10} \overline{C^*}$), T_{max} , signal-weighted average values of elemental
 1024 composition, carbon oxidation state ($\overline{OS_c}$), H:C, O:C, N:C for all FIGAERO-OA factors. The
 1025 estimation of $\overline{OS_c}$ can be found in Section S2. The volatility of each FIGAERO-OA factor was
 1026 estimated based on their corresponding T_{max} using eq. (8) and (9).

	$\log_{10} \overline{C^*}$ ($\mu\text{g m}^{-3}$)	T_{max} ($^{\circ}\text{C}$)	Average elemental composition	$\overline{OS_c}$	H:C	O:C	N:C
Day-HNO _x - LVOA	-0.98	84.52	$\text{C}_{7.37}\text{H}_{10.51}\text{O}_{4.99}\text{N}_{0.36}$	-0.01	1.37	0.75	0.06
Day-LNO _x - LVOA	-2.71	103.29	$\text{C}_{6.52}\text{H}_{8.77}\text{O}_{4.54}\text{N}_{0.22}$	0.18	1.35	0.80	0.04
Day-aged- LVOA	-2.02	95.53	$\text{C}_{6.35}\text{H}_{8.75}\text{O}_{5.13}\text{N}_{0.21}$	0.35	1.42	0.91	0.04
Day-aged- ELVOA	-4.80	126.65	$\text{C}_{5.22}\text{H}_{7.36}\text{O}_{4.20}\text{N}_{0.16}$	0.40	1.55	1.00	0.03
Day-urban- LVOA	-0.90	83.03	$\text{C}_{6.50}\text{H}_{9.27}\text{O}_{4.71}\text{N}_{0.24}$	0.08	1.43	0.80	0.04
Day-urban- ELVOA	-7.18	153.22	$\text{C}_{6.57}\text{H}_{8.54}\text{O}_{4.61}\text{N}_{0.24}$	0.26	1.35	0.84	0.05
BB-LVOA	-2.36	99.39	$\text{C}_{6.72}\text{H}_{9.78}\text{O}_{4.61}\text{N}_{0.26}$	-0.08	1.47	0.74	0.04
Night-LVOA	-2.02	95.53	$\text{C}_{7.69}\text{H}_{11.04}\text{O}_{5.19}\text{N}_{0.47}$	-0.09	1.47	0.77	0.07

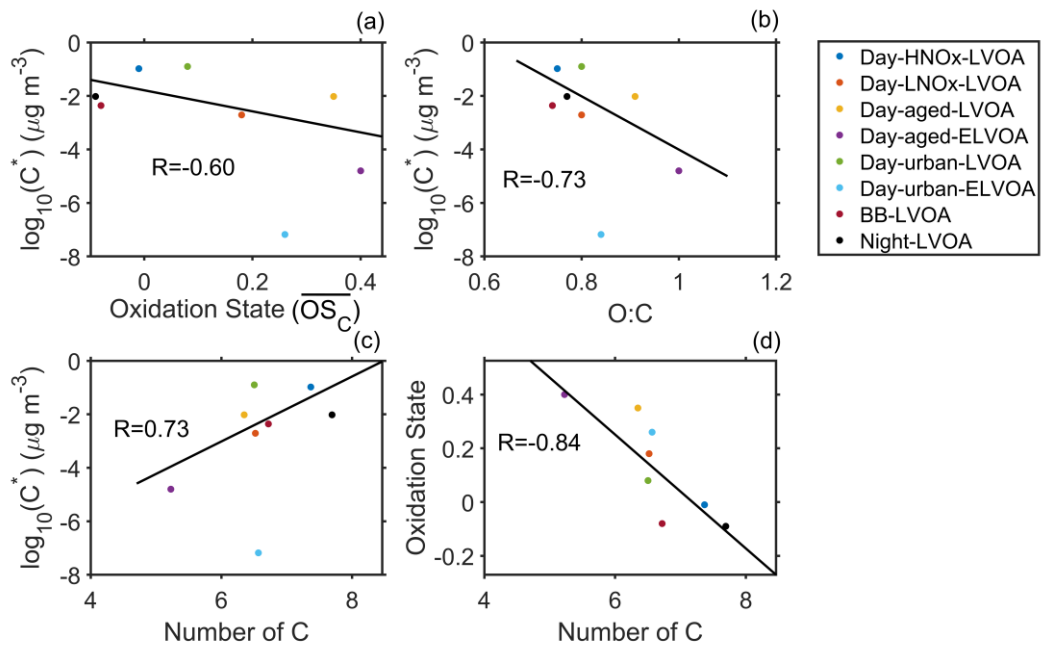
1027



1028

1029 **Figure 1.** Diurnal variation (a1 to h1), mass spectra (a2 to h2), and thermograms (a3 to h3) of
1030 FIGAERO-OA factors.

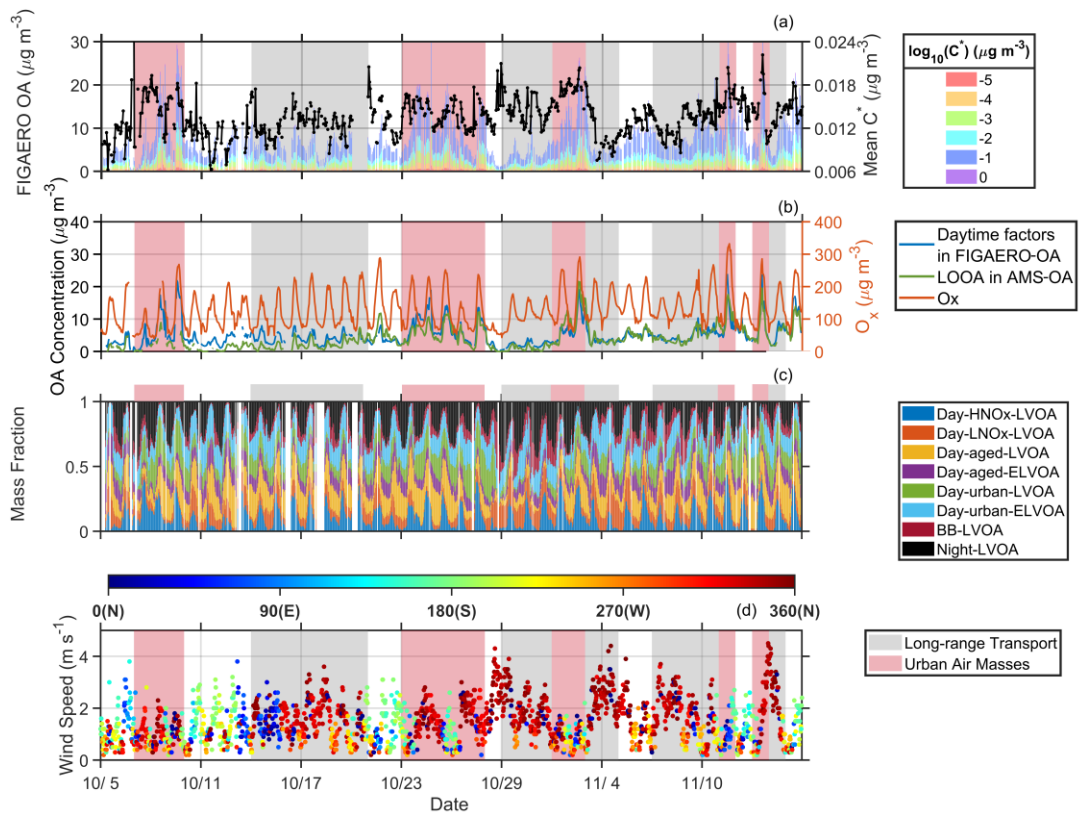
1031



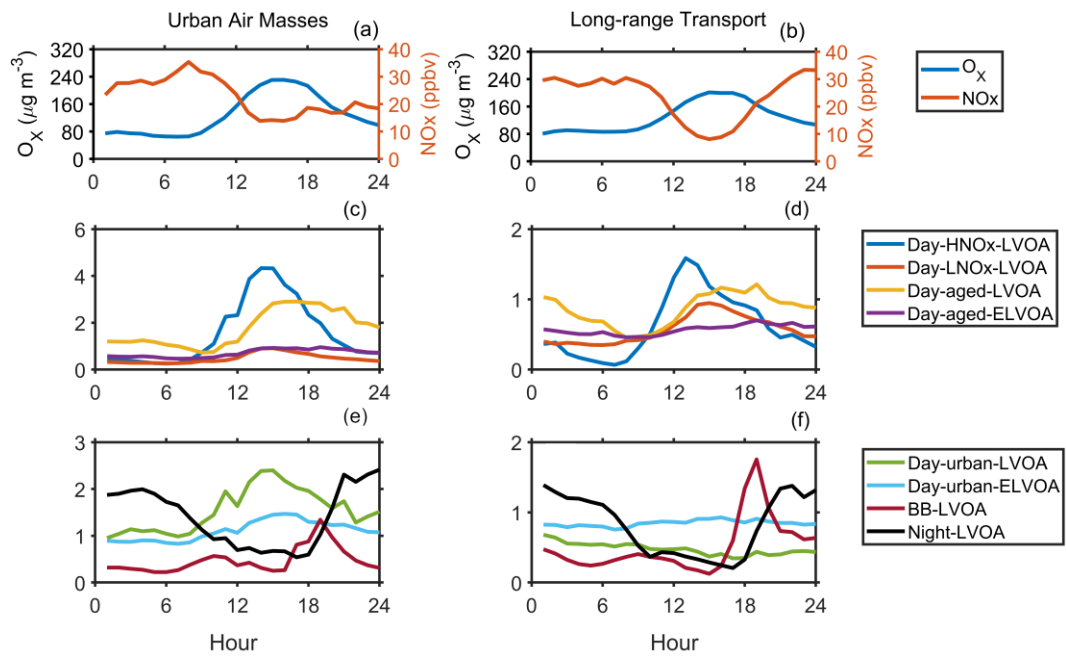
1032

1033 **Figure 2.** The average volatility of FIGAERO-OA factor vs. (a) oxidation state (\overline{OS}_c), (b) O:C ,
 1034 and (c) number of carbons and (d) Number of carbons vs. \overline{OS}_c of thermogram factor. Day-urban-
 1035 ELVOA is excluded in the estimation of R.

1036

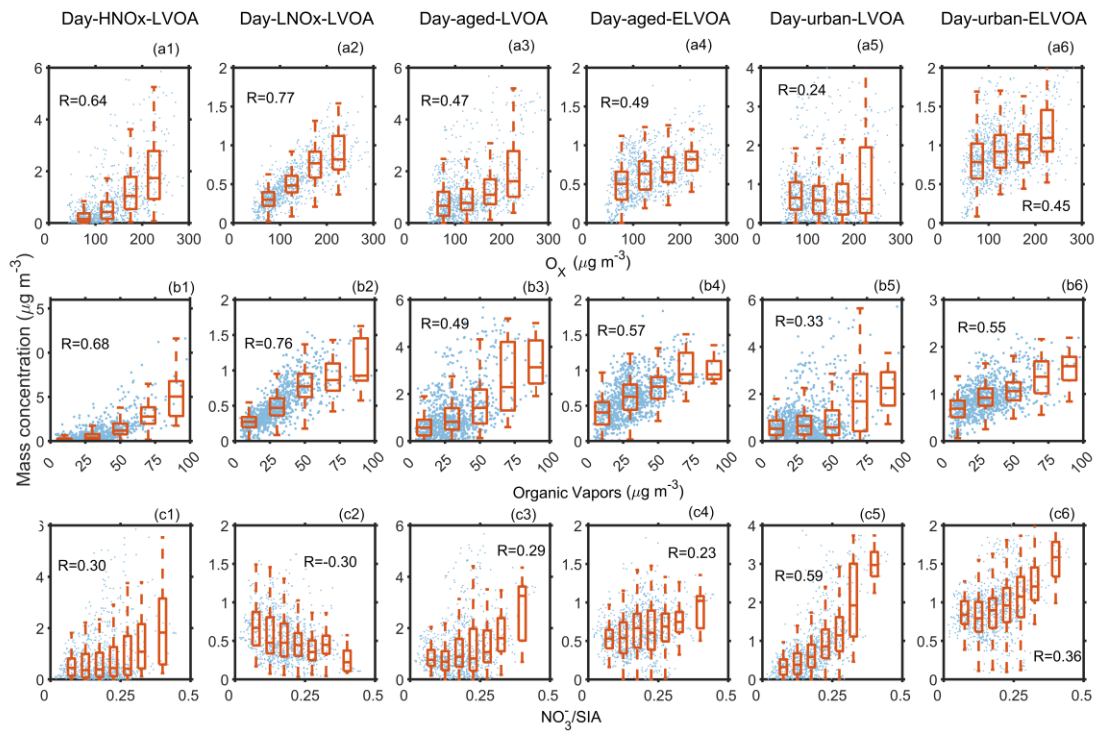


1039 **Figure 3.** Time series of (a) volatility (presented in a range from 10^{-5} to $10^0 \mu\text{g m}^{-3}$) of FIGAERO-
 1040 OA and mean C^* , (b) daytime factors (Day-HNO_x-LVOA, Day-LNO_x-LVOA, Day-aged-LVOA,
 1041 Day-aged-ELVOA, Urban LVOA, and Day-urban-ELVOA) in FIGAERO-OA and LOOA factor
 1042 from PMF analysis of SP-AMS data, (c) mass fraction of eight FIGAERO-OA factors, and (d) wind
 1043 speed and wind direction.



1047 **Figure 4.** The average diurnal variation of O_x , NO_x , and mass concentration of eight thermogram
 1048 factors during the long-range transport (a, c, and e) and urban air masses (b, d, and f) period.
 1049

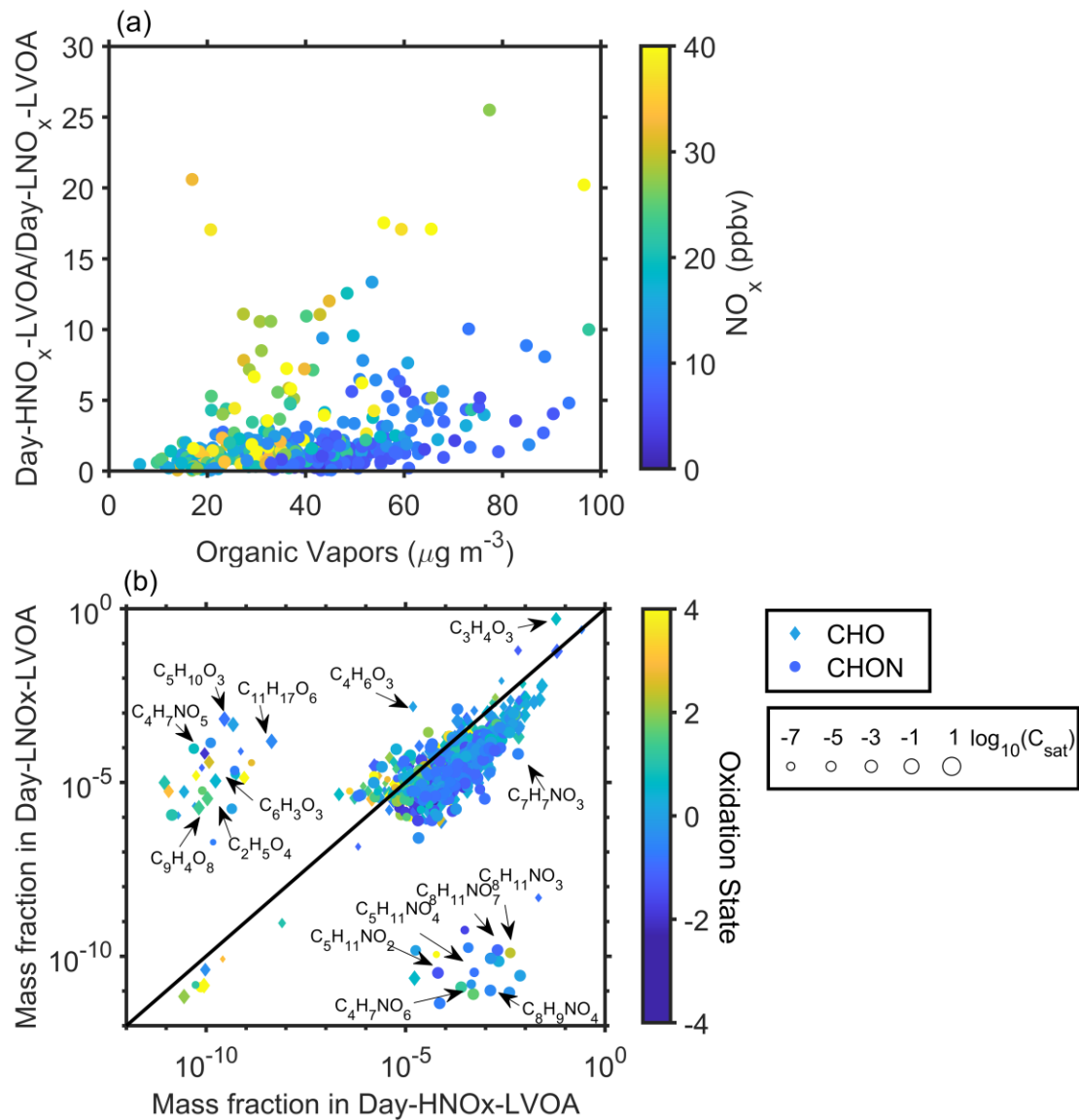
1050



1051

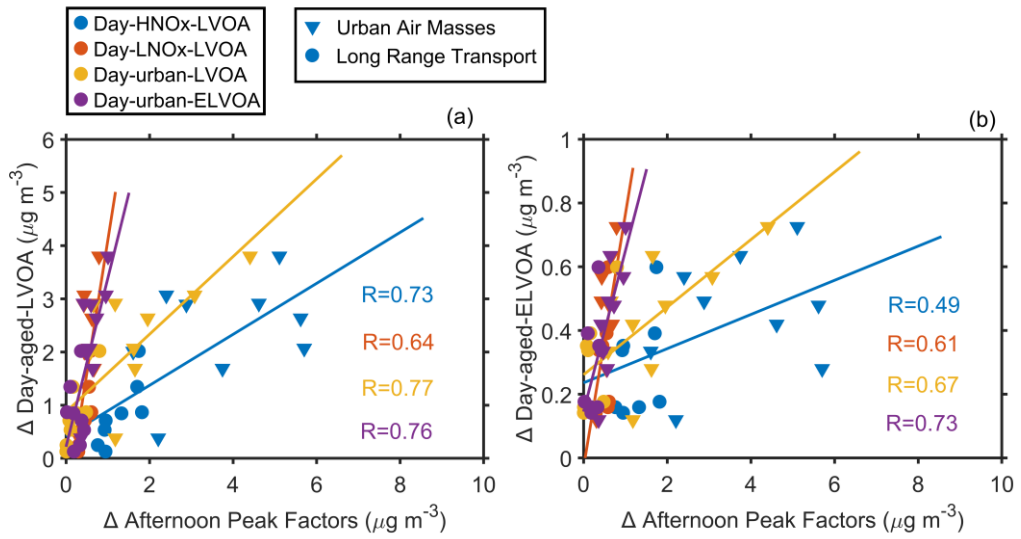
1052 **Figure 5.** Relationship between the mass concentration of six daytime thermogram factors and
 1053 (a1-6) O_x , (b1-6) organic vapors, (c1-6) nitrate fraction in secondary inorganic aerosol (SIA), and
 1054 (d1-6) sulfate fraction in SIA measured by the FIGAERO-CIMS. The organic vapors are the sum
 1055 of organic compounds in the gas-phase measured by the FIGAERO-CIMS.

1056



1057

1058 **Figure 6.** (a) Correlation between organic vapors and the ratio of Day-HNO_x-LVOA to Day-LNO_x-
 1059 LVOA. (b) Scatterplots of mass fraction of different species in Day-HNO_x-LVOA and Day-LNO_x-
 1060 LVOA. The color of dots in panel (a) denotes the corresponding NO_x. The shape, size, and color of
 1061 markers in panel (b) represents the class of species, volatility, and \overline{OS}_C , respectively.
 1062



1065 **Figure 7.** Correlation between the enhancement of (a) Day-aged-LVOA and afternoon peak factors
 1066 and (b) Day-aged-ELVOA and afternoon peak factors. Afternoon peak factors include Day-HNO_x-
 1067 LVOA, Day-LNO_x-LVOA, Day-urban-LVOA, and Day-urban-ELVOA. For afternoon peak factors,
 1068 the enhancement (Δ) was regarded as the average mass concentration during 00:00-6:00 LT and
 1069 12:00-18:00 LT. For Day-aged-LVOA and Day-aged-ELVOA, the enhancement (Δ) was estimated
 1070 as the difference between average mass concentration during 00:00-6:00 LT and 12:00-18:00 LT.
 1071

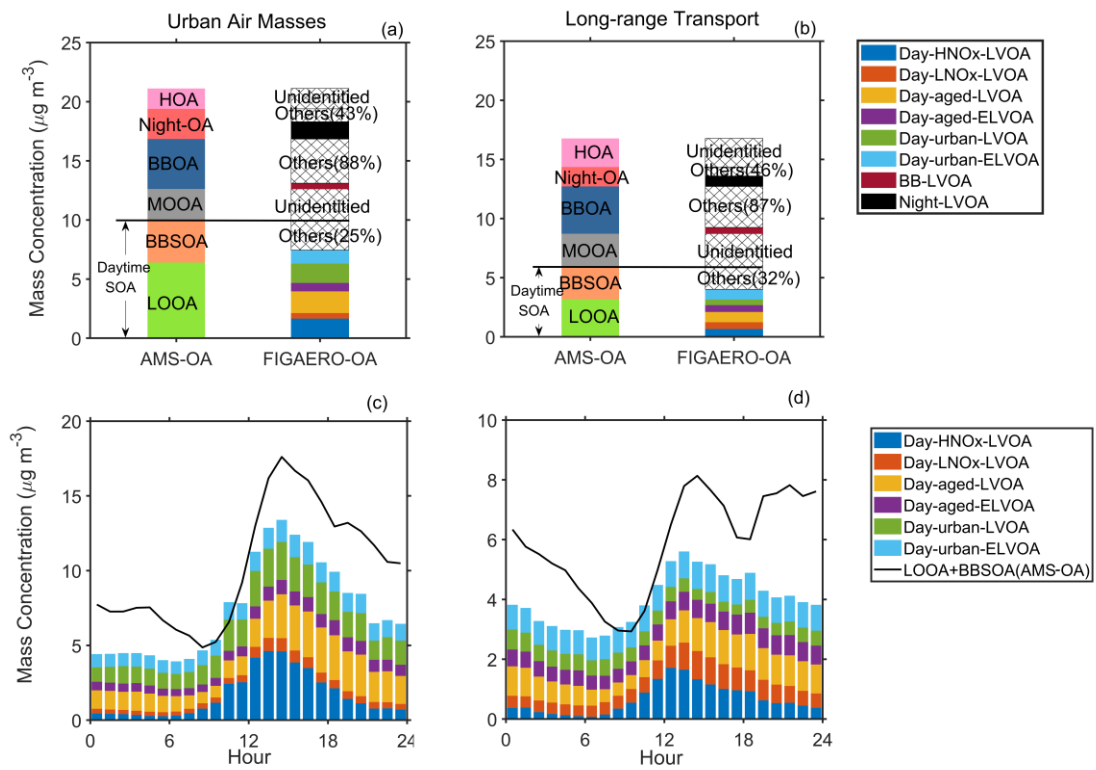
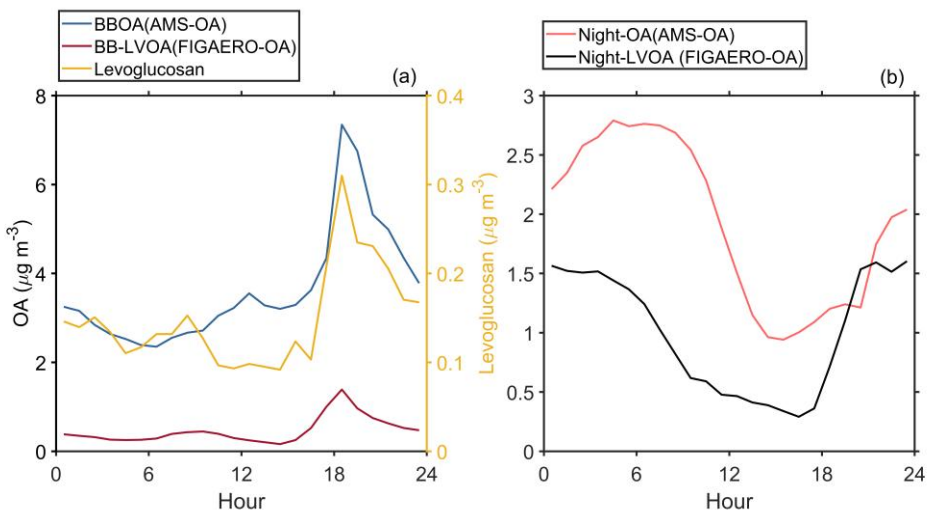


Figure 8. Comparison of the average mass concentration (a and b) and diurnal variation (c and d) of AMS-OA and FIGAERO-OA during long-range transport and urban air masses period.



1079 **Figure 9. (a)** Diurnal variation of BBOA from AMS, BB-LVOA and levoglucosan from FIGAERO-
 1080 CIMS;(b) Diurnal variation of Night-OA from AMS, and Night-LVOA from FIGAERO-CIMS.